

1 **Extreme Concentric Gravity Waves Observed in the Mesosphere**
2 **and Thermosphere Regions over Southern Brazil Associated with**
3 **Fast-Moving Severe Thunderstorms**

4 Qinzeng Li¹, Jiyao Xu¹, Yajun Zhu¹, Cristiano M. Wrasse², José V. Bageston³, Wei
5 Yuan¹, Xiao Liu⁴, Weijun Liu¹, Ying Wen⁵, Hui Li¹, and Zhengkuan Liu¹

6

7 1. State Key Laboratory of Solar Activity and Space Weather, National Space Science Center,
8 Chinese Academy of Sciences, Beijing, 100190, China

9 2. National Institute for Space Research, Space Weather Division, São José dos Campos, SP,
10 Brazil

11 3. National Institute for Space Research, Southern Space Coordination, Santa Maria, RS, Brazil

12 4. School of Mathematics and Information Science, Henan Normal University, Xinxiang,
13 453007, China

14 5. College of Aviation Meteorology, Civil Aviation Flight University of China, Guanghan,
15 618307, China

16 Correspondence: Jiyao Xu (jyxu@swl.ac.cn) and Yajun Zhu (y.zhu@swl.ac.cn)

17 **Abstract**

18 Three groups of intense concentric gravity waves (CGWs) lasting over 10 hours
19 were observed by an airglow imager at the Southern Space Observatory (SSO) in São
20 Martinho da Serra (29.44°S, 53.82°W) in southern Brazil on 17-18 September 2023.
21 These CGW events were simultaneously captured by spaceborne instruments,
22 including the Atmospheric Infrared Sounder (AIRS) aboard Aqua, the Visible
23 Infrared Imaging Radiometer Suite (VIIRS) onboard Suomi NPP, and the Sounding
24 of the Atmosphere using Broadband Emission Radiometry (SABER) instrument
25 operating on the Thermosphere-Ionosphere-Mesosphere Energetics and Dynamics
26 (TIMED) satellite. The CGW caused significant airglow radiation perturbations
27 exceeding 24% and the distance of the wave center movement exceeded 400 km.
28 These CGW events were caused by fast-moving deep convection observed by
29 Geostationary Operational Environmental Satellite-16 (GOES-16). The weaker
30 background wind field during the spring season transition provides the necessary
31 conditions for CGWs to propagate from the lower atmosphere to the mesopause
32 region. The 630 nm emission images were significantly contaminated by specific
33 OH emission bands. The same CGW event was observed propagating from the OH
34 airglow layer (~87 km) to the thermospheric OI 630.0 nm airglow layer (~250 km).
35 The asymmetric propagation of CGWs in the thermosphere may be due to the vertical
36 wavelength changes caused by the Doppler-shifting effect of the background wind
37 field. This multi-layer ground-based and satellite joint detection of CGWs offers
38 an excellent perspective for examining the coupling of various atmospheric layers.

39 **1. Introduction**

40 Atmospheric gravity waves (AGWs) are disturbances in the atmosphere
41 caused by various sources, such as convection (Fovell et al. 1992; Piani et al. 2000;
42 Heale et al., 2021; Franco-Diaz et al., 2024), front/jet stream (Fritts and Nastrom,
43 1992; Plougonven and Zhang 2014; Dalin et al., 2016; Wrasse et al., 2024), wind
44 shear (Fritts, 1982; Pramitha et al., 2015), orography forcing (Nastrom and Fritts,
45 1992; Wright et al., 2017; Liu et al., 2019; Heale et al., 2020; Geldenhuys et al.,
46 2021; Inchin et al., 2024), and air–sea interaction (Li et al., 2024). AGWs are
47 generated when strong updrafts and downdrafts displace the stable stratification
48 of the atmosphere. As AGWs propagate vertically from the lower atmosphere,
49 their amplitude grows markedly owing to reduced density. When they reach
50 mesosphere–lower thermosphere (MLT) altitudes, they become unstable and
51 break, dissipating momentum and energy into the surrounding atmosphere (Cao
52 and Liu, 2016; Ern et al., 2022). This energy deposition makes AGWs crucial
53 drivers of the momentum and energy budgets in the MLT region, fundamentally
54 governing the general circulation, thermal structure, chemical composition
55 distribution, and transport regimes (Fritts and Alexander, 2003; Plane et al., 2023).

56 Among the many sources of AGWs, convective sources are particularly
57 significant (Alexander and Holton, 2004). They can generate concentric gravity
58 waves (CGWs), the source location of which can be readily determined by the
59 center position. The backward ray tracing method, employed for source location
60 determination, can also be applied to circular gravity wave patterns (Ern et al. 2022).

61 This enables point-to-point studies of their propagation characteristics. The
62 release of latent heat in deep convection acts as a forcing mechanism (Lane et al.,
63 2001), creating CGWs that can propagate upward into the middle and upper
64 atmosphere.

65 All-sky airglow imagers provide a large field of view and high-resolution
66 observations, making them particularly suitable for observing short-period AGWs
67 in the mesosphere and thermosphere. Through the observational data from airglow
68 imagers, researchers can analyze the propagation characteristics of AGWs,
69 including parameters such as horizontal wavelengths, observed periods,
70 horizontal phase velocities and momentum fluxes (Swenson and Liu, 1998).

71 Although the observation of AGWs by airglow imagers has been widely
72 documented in previous studies (Dalin et al., 2024; Nyassor et al., 2021, 2022;
73 Suzuki et al., 2007a; Vadas et al., 2012; Vargas et al., 2021; Wüst et al., 2019; Xu
74 et al., 2015; Yue et al., 2009), dual-layer airglow observations, which involve
75 observing airglow emissions from a hydroxyl radical (OH) layer (~ 87 km) in the
76 mesosphere and an atomic oxygen emission layer at 630 nm (OI 630.0 nm) (~ 250
77 km) in the thermosphere, offer a unique opportunity to simultaneously investigate
78 CGWs in both the mesosphere and thermosphere. This configuration enables
79 comprehensive studies of gravity wave vertical propagation and their role in
80 vertical atmospheric coupling. However, due to past limitations in observational
81 capabilities, simultaneous detection of CGWs across both the OH and OI 630.0 nm
82 layers was rare.

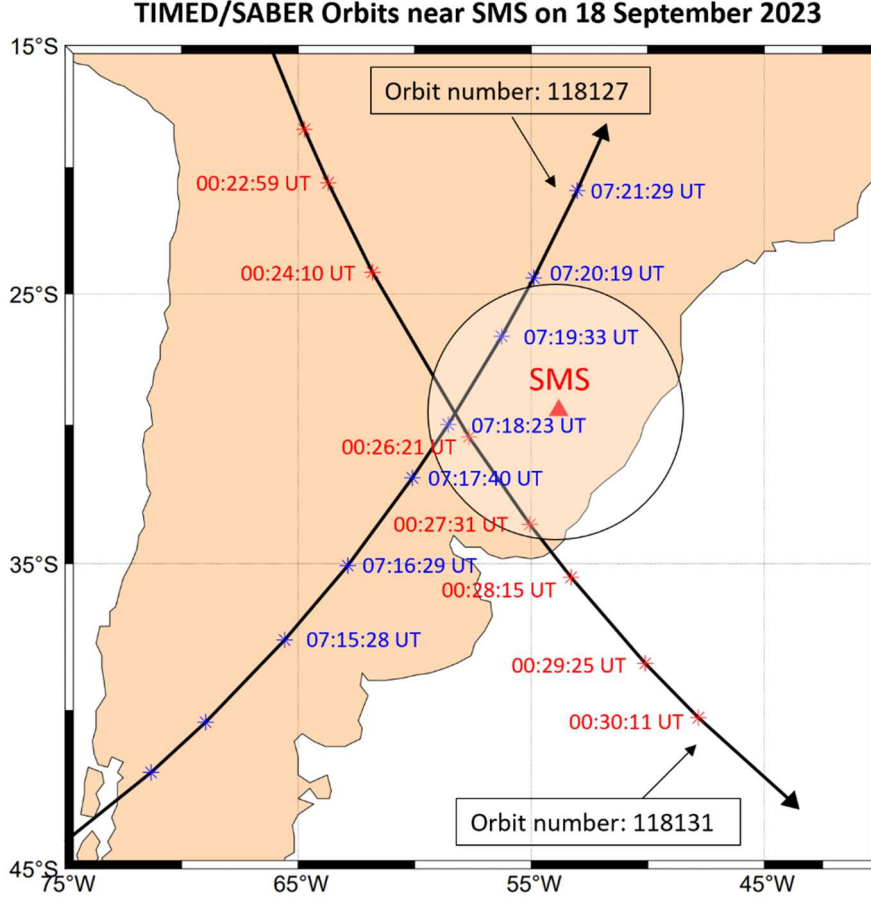
83 In this study, we observed multiple strong CGW events using airglow
84 measurements in southern Brazil on 17-18 September 2023, with a maximum
85 amplitude reaching 24%, which is far higher than previously reported events with
86 average amplitudes of 2-3% (Li et al., 2016; Tang et al., 2014; Suzuki et al.,
87 2007a). Through ground-based dual-layer and multi-satellite joint observations,
88 we conducted a comprehensive analysis of these events to reveal their role in
89 vertical energy transfer and atmospheric coupling.

90 **2. Ground based Airglow Imager and Satellite observation**

91 **2.1 Airglow Imager**

92 The airglow imager used to observe CGW is installed at the Southern Space
93 Observatory (SSO), the National Institute for Space Research, in São Martinho da
94 Serra (SMS) (29.44°S, 53.82°W), Brazil. Figure 1 shows the location of the
95 airglow imager station at SMS. The imager has a cooled Charge-Coupled Device
96 (CCD) camera with a Mamiya (Focal Length = 24 mm) fish-eye lens of a 180°
97 field of view (FOV) and a resolution of 512×512 pixels. The imager is equipped
98 with a filter wheel, and the wheel rotates to observe OH (Wüst et al., 2023)
99 broadband emission (715–930 nm, with a notch at 865.5 nm to suppress the O₂(0,
100 1) emission) and O(¹D) (630.0 nm, 2.0 nm), respectively. The time resolution of
101 the OH airglow image is 112 s, while that of the OI 630 nm airglow image is 225
102 s. The exposure times of the OH airglow image and the OI 630 nm airglow image are
103 20 s and 90 s, respectively. Airglow observations are conducted when the solar
104 depression angle is less than -12° .

105



107

108 **Figure 1.** The location of the airglow imager station at SMS (red triangle). The circle on the map
 109 gives the effective observation ranges of OH airglow imager with a 164° field of view. The red
 110 asterisks and blue asterisks denote the TIMED/SABER ascending and descending track footprints
 111 passing over SMS on 18 September 2023, respectively.

112 Before effectively extracting the wave parameters, the raw airglow images need
 113 to be processed through the following steps: First, a median filter with a kernel size
 114 of 17×17 pixels was employed to eliminate stars from the raw images (Li et al.,
 115 2011). We also removed the CCD dark noise, which was estimated from dark-frame
 116 images captured with the shutter closed prior to observations. Second, we corrected
 117 for the van Rhijn effect and atmospheric extinction using the approach described in
 118 Kubota et al. (2001). The observed airglow intensity $I(\theta)$ from the ground is not

119 uniform across different zenith angles. This non-uniformity is due to the van Rhijn
 120 effect. Additionally, the observed airglow intensity is influenced by atmospheric
 121 extinction, which results from absorption and scattering along the line of sight.

122 Since airglow observations are subject to the van Rhijn effect, the measured
 123 emission intensity at a specific zenith angle (θ) follows the relation (Kubota et al.,
 124 2001):

$$125 \quad I(\theta) = I(0) \cdot V(H, \theta),$$

$$V(H, \theta) = \left[1 - \left(\frac{R}{R+H} \right)^2 \sin^2(\theta) \right]^{-1/2}, \quad (1)$$

126 where $I(0)$ is the emission intensity at zenith. $V(H, \theta)$ is the van Rhijn correction
 127 factor. R is the earth radius and H is the height of OH airglow layer. The relationship
 128 between the observed emission intensity $I(\theta)$ —affected by atmospheric extinction—
 129 and the true emission intensity $I_{true}(\theta)$ at the airglow layer is described by Kubota
 130 et al. (2001).

$$131 \quad I(\theta) = I_{true}(\theta) \cdot 10^{-0.4 \cdot a \cdot F(\theta)},$$

$$F(\theta) = \left[\cos \theta + 0.15 \cdot \left(93.885 - \theta \cdot \frac{180}{\pi} \right)^{-1.253} \right]^{-1}, \quad (2)$$

132 where a is the atmospheric extinction coefficient, $F(\theta)$ is an empirical equation.

133 Consequently, the image correction factor, obtained from the combination of
 134 Eqs. (1) and (2), takes the form:

$$135 \quad K = V(H, \theta) \cdot 10^{-0.4 \cdot a \cdot F(\theta)}. \quad (3)$$

136 The parameter a depends on the atmospheric observing conditions. For the observed
 137 CGW events, we treat a as temporally constant. By averaging the images over the
 138 observation period, we derive the zenith-angle-dependent airglow intensity profile.

139 The optimal value of a is determined by matching this observed profile with
 140 theoretical K profiles across varying a . The fitted value of parameter a is
 141 approximately 0.42. Finally, we apply the flat-field correction by dividing the raw
 142 images by the corresponding K factor.

143 Third, we eliminated atmospheric background counts from the images. For
 144 background emission, Swenson and Mende (1994) used simultaneous Infrared
 145 measurements to demonstrate that the background contributes approximately 30% of
 146 the total OH airglow image signal. Similarly, Suzuki et al. (2007b) confirmed this
 147 ratio (~30%) through concurrent OH intensity observations with a Spectral Airglow
 148 Temperature Imager. In this study, we adopt the same assumption that background
 149 emissions account for ~30% of the total signal.

150 Then, the original airglow images were spatially calibrated using stars as
 151 reference points. Each pixel location (i, j) in the original image was first mapped to a
 152 position (f, g) in a standardized coordinate system. Subsequently, the point (f, g) was
 153 transformed into geographic coordinates (x, y) using azimuth (az) and elevation (el)
 154 angles.

155 The conversion between original image coordinates (i, j) and standard
 156 coordinates (f, g) is defined by a linear transformation (Hapgood and Taylor, 1982):

$$157 \quad \begin{bmatrix} f \\ g \end{bmatrix} = \begin{bmatrix} a_0 & a_1 & a_2 \\ b_0 & b_1 & b_2 \end{bmatrix} \begin{bmatrix} 1 \\ i \\ j \end{bmatrix}, \quad (4)$$

158 where the coefficients a and b are calculated by applying a least-squares fitting using
 159 the observed location of the stars in the original image and their locations in standard

coordinate (Garcia et al., 1997):

$$\begin{bmatrix} a_0 & b_0 \\ a_1 & b_1 \\ a_2 & b_2 \end{bmatrix} = \begin{bmatrix} \mathbf{1}^T \mathbf{1} & \mathbf{1}^T \mathbf{i} & \mathbf{1}^T \mathbf{j} \\ \mathbf{1}^T \mathbf{i} & \mathbf{i}^T \mathbf{i} & \mathbf{i}^T \mathbf{j} \\ \mathbf{1}^T \mathbf{j} & \mathbf{i}^T \mathbf{j} & \mathbf{j}^T \mathbf{j} \end{bmatrix}^{-1} \begin{bmatrix} \mathbf{1}^T \\ \mathbf{i}^T \\ \mathbf{j}^T \end{bmatrix} \begin{bmatrix} \mathbf{f} & \mathbf{g} \end{bmatrix}, \quad (5)$$

where the column vectors \mathbf{i} and \mathbf{j} contain observed star locations in the original image, while \mathbf{f} and \mathbf{g} hold their computed normalized coordinates. The vector $\mathbf{1}$ is a constant-valued column vector with length matching these vectors.

Through a georeference procedure, the standard coordinate images were projected onto geographic coordinates, assuming peak emission heights of 87 km for the OH layer and 250 km for the OI 630.0 nm layer. The spatial resolution of the imager varies significantly zenith angle. For the OH channel, it is 0.53 km/pixel at the center of the image and degrades to 39.8 km/pixel at the edge of the image. For the 630 channel, the resolution is 1.53 km/pixel at the center of the image and decreases to 40.8 km/pixel at the edge of the image.

2.2 GOES, Aqua, Suomi NPP, and TIMED Satellite Observations

2.2.1 GOES Satellite Observations

The Geostationary Operational Environmental Satellite-16 (GOES-16) (Schmit et al., 2005), launched in November 2016, is part of the GOES-R Series. The Advanced Baseline Imager (ABI) is the primary instrument on GOES-16, providing high-resolution imagery in 16 spectral bands, including 2 visible channels (0.47 μm and 0.64 μm), 4 near-infrared channels (0.86 μm , 1.37 μm , 1.6 μm , and 2.2 μm), and 10 infrared channels (3.9–13.3 μm), with a temporal resolution of 10 min and a spatial resolution of 0.5–2 km (Schmit et al., 2017). The brightness temperature (BT), derived from 10.3 μm infrared images from channel 13, is used

182 to study the convection activities during the CGW events.

183 **2.2.2 Aqua Satellite Observations**

184 The Atmospheric Infrared Sounder (AIRS) (Aumann et al., 2003; Chahine et al.,
185 2006) is an infrared spectrometer and sounder onboard the NASA Aqua satellite
186 (Parkinson et al., 2003). AIRS performs continuous across-track scanning, acquiring
187 data footprints sequentially. The collected data are then organized into 6-minute
188 granules. The footprint size of AIRS is approximately 13–14 km in diameter at nadir
189 view, and the scan swath width is around 1765 km (Hoffmann et al., 2014). AIRS
190 is capable of detecting air thermal perturbations induced by GWs with vertical
191 wavelengths longer than 10–15 km and horizontal wavelengths ~ 50 –500 km
192 (Hoffmann and Alexander, 2010). The radiance measurements at the $4.3\ \mu\text{m}$ CO₂
193 fundamental emission band are particularly sensitive at altitudes around 30–40 km.
194 In this study, the CO₂ radiance emission band with frequencies ranging between
195 $2299.80\ \text{cm}^{-1}$ and $2422.85\ \text{cm}^{-1}$ (Rothman et al., 2013) is utilized to measure
196 stratospheric air temperature perturbations.

197 **2.2.3 Suomi NPP Satellite Observations**

198 The Visible Infrared Imaging Radiometer Suite (VIIRS) instrument, onboard
199 the Suomi NPP satellite (Lee et al., 2010; Lewis et al., 2010), is a multispectral
200 scanner capable of capturing high-resolution images in both visible and infrared
201 wavelengths. The Day Night Band (DNB) of the VIIRS sensor operates in the
202 visible/near-infrared (NIR) range, covering wavelengths from 500 to 900 nm
203 (Miller et al., 2012), which includes three key mesospheric airglow emissions: the

204 O(1S) line at 557.7 nm, the Na doublet at 589.0/589.6 nm, and the OH Meinel
205 band (~600–900 nm). The sensor has a high spatial resolution of 0.375 km at nadir
206 for its imagery bands and 0.75 km for its moderate-resolution bands. The VIIRS
207 sensor has a wide across-track swath width of 3000 km.

208 **2.2.4 TIMED Satellite Observations**

209 Sounding of the Atmosphere using Broadband Emission Radiometry (SABER)
210 is one of four instruments on NASA's Thermosphere Ionosphere Mesosphere
211 Energetics Dynamics (TIMED) satellite (Russell et al., 1999), launched on December
212 7, 2001. TIMED focuses on exploring the energy properties and redistribution in the
213 MLT region, providing data to define the basic states and thermal balance of this area.
214 SABER is a 10-channel broadband limb-scanning infrared radiometer (1.27-17 μm).
215 It measures kinetic temperature through CO₂ emissions (15 μm Local
216 Thermodynamic Equilibrium (LTE) below 90 km; 4.3 μm non-LTE above 90 km)
217 with ± 2 -5 K accuracy. Simultaneously observing O₃ (9.6 μm), OH (1.6-2.0 μm), and
218 O₂ (1.27 μm) emissions, it quantifies radiative cooling (up to 150 K/day) and chemical
219 heating (~ 8 K/day) in the MLT region with 2-4 km vertical resolution.

220 **3 Observations**

221 **3.1 Double-layer All sky Airglow Imager Observations**

222 **3.1.1 Mesospheric Concentric Gravity Waves from OH All sky imaging** 223 **observation**

224 Three groups of intense CGWs (wave packets nos. 1–3) were captured by the
225 OH emission channel of the airglow imager at the Southern Space Observatory (SSO)
226 in São Martinho da Serra (29.44°S, 53.82°W) in southern Brazil on 17-18 September
227 2023. These events initially emerged within the imager's field of view at 22:25:02 UT

228 on 17 September and remained continuously detectable until the cessation of
229 observational recording at 08:35:15 UT on 18 September, thereby spanning an
230 extended duration in excess of 10 hours. For more detailed information on the wave
231 propagation status, please refer to the Supplement (<http://doi.org/10.5446/69990>, Li,
232 2025a). Figure 2 shows the time sequence of CGW no. 1 from 22:49:23 UT on 17
233 September to 03:39:31 UT on 18 September. CGW no. 1 first appeared in the
234 southwest direction of the station.

235 The distinct visible concentric wavefronts radiating outward from the center (red
236 dot in each panel) are indicative of the atmospheric response to disturbances caused
237 by strong convection in the lower atmosphere. Interestingly, the center of CGW no. 1
238 continues to move eastward. Between 22:45:38 UT on 17 September and 05:26:13
239 UT on 18 September, the center moved approximately 436 km eastward, with an
240 average speed reaching ~ 65 km/h. This eastward drift of the wave's center could be
241 indicative of the influence of prevailing wind patterns and the eastward movement of
242 the convective system itself. The horizontal wavelengths of the GWs at radii of 0–
243 300 km (denoted by the red line in Fig. 2 at 23:39:55 UT) are measured to be (30–82)
244 ± 3 km. The observed period is 9.0 ± 3.5 min, and the observed phase speed is 80–
245 110 ms^{-1} . In the northwest direction (denoted by the red line in Fig. 2 at 00:49:11 UT),
246 we have detected larger-scale waves with a wavelength of about 160 km, a period of
247 approximately 16 min, and a phase speed of about 167 ms^{-1} .

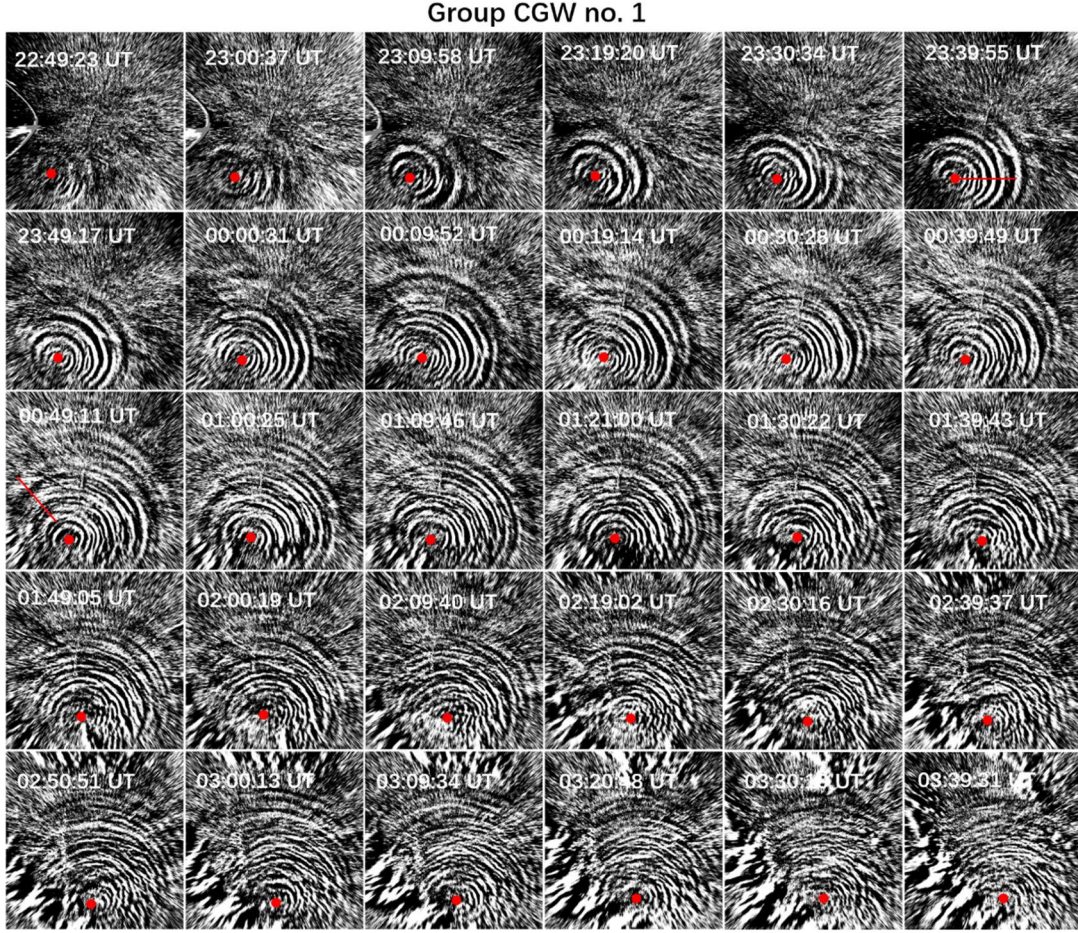


Figure 2. All-sky OH images projected onto an area of 1000 km×1000 km showing the CGW no.1 event at half-hour intervals in the SMS station on 17-18 September 2023. The red dots mark the estimated centers of the CGW. The presented images display the corrected OH emission intensity.

From 02:00 UT, clouds began forming in the southwestern and western sectors of the station (see Fig. 2). By 04:00 UT, cloud formation extended to the zenith and northern sectors, persisting until ~05:30 UT. Figure 3 shows the time sequence of CGW no. 2 and CGW no. 3 from 03:58:14 UT on 17 September to 07:59:42 UT on 18 September. Despite cloud cover, CGW no. 2 and CGW no. 3 were observed in cloud gaps over the western sector at approximately 03:45:08 UT and 05:13:06 UT, respectively. For CGW no. 2, horizontal wavelengths range from 22 to 38 km, with a period of 7 ± 1.5 min and a phase speed of 60–78 ms^{-1} . CGW no. 3 exhibits

wavelengths of 24–36 km, a period of 6.5 ± 1.0 min, and a phase speed of $72\text{--}81\text{ ms}^{-1}$.

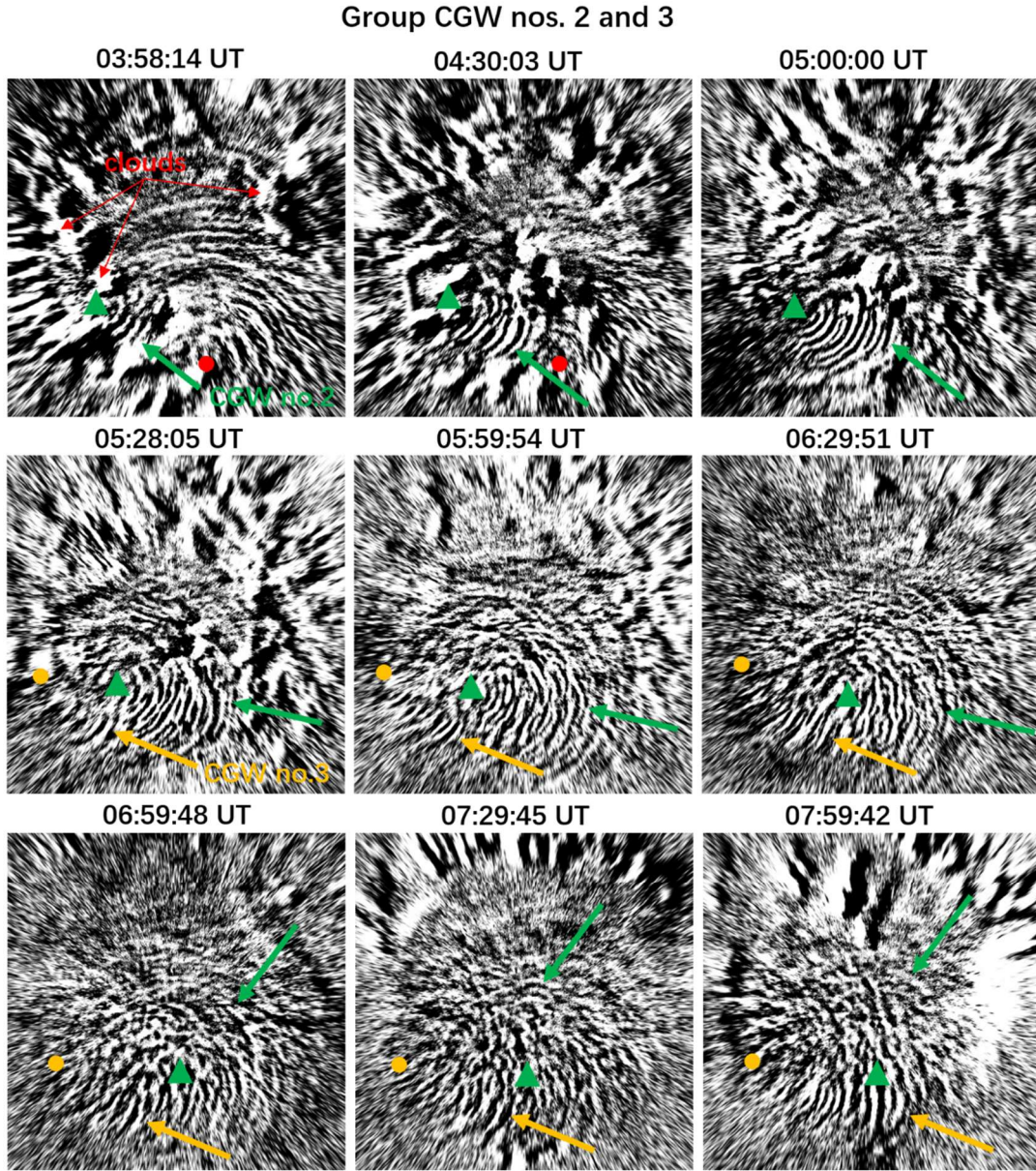
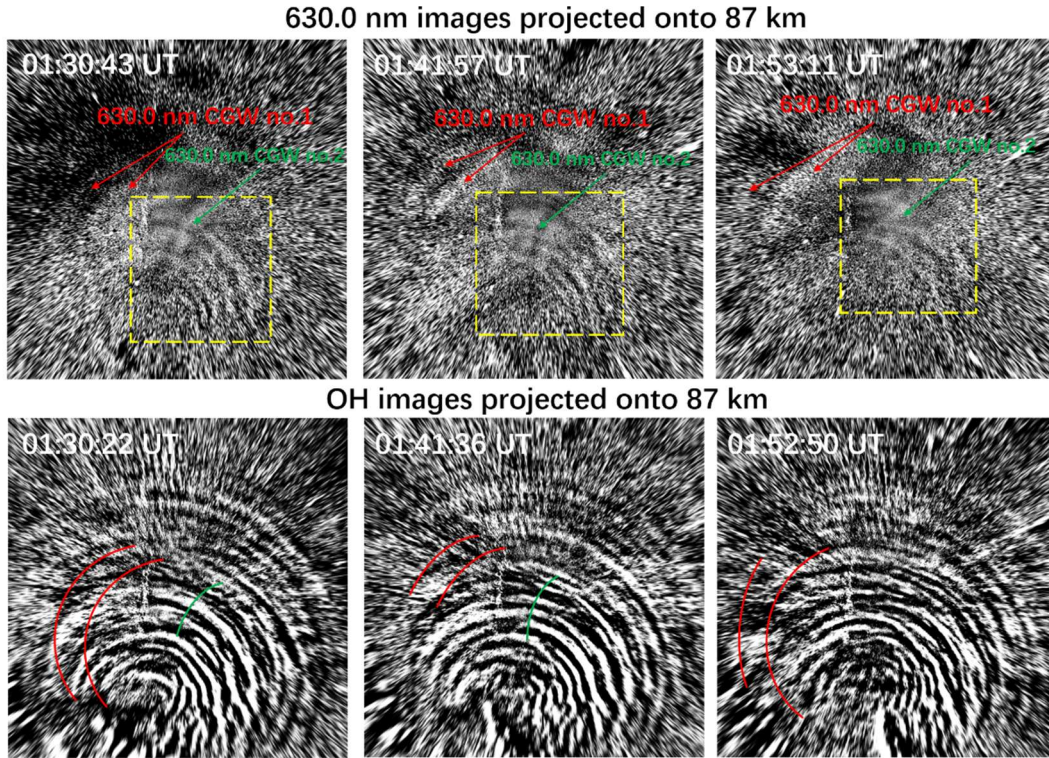


Figure 3. All-sky OH images projected onto an area of $1000\text{ km} \times 1000\text{ km}$ showing the CGW no. 2 and CGW no. 3 events at half-hour intervals in the SMS station on 18 September 2023. The red dot marks the estimated center of the CGW no. 1, while the green and light blue dots indicate the estimated centers of the CGW no. 2 and CGW no. 3, respectively. The presented images display the corrected OH emission intensity.

3.1.2 Thermospheric Concentric Gravity Waves from All sky 630.0 nm imaging observation

The 630.0 nm filter used in the imager is a narrowband interference filter with a

central wavelength of 630.0 nm and a full-width at half-maximum (FWHM) spectral width of 2.0 nm. Three spectral lines from the OH (9–3) band lie within the bandwidth of the 630.0 nm filter: the P2(3) line at 629.7903 nm, the P1(3) doublet at 630.6869 nm and 630.6981 nm, and the P1(2) line at 628.7434 nm (Hernandez, 1974; Burnside et al., 1977; Smith et al., 2013). To determine whether the OI 630 nm airglow image is contaminated by OH airglow emission, we project both the OH airglow image and the OI 630 nm airglow image onto the height of the OH airglow layer. We can clearly see that the OI 630 nm airglow image is contaminated by OH emission, with the CGWs observed in the OH airglow layer being superimposed onto the OI 630 nm airglow image denoted by the yellow dashed boxes in Fig. 4. Thus, we must exercise extreme caution when interpreting disturbances in the thermosphere observed at the 630 nm wavelength, particularly in the absence of concurrent OH airglow measurements to differentiate whether these disturbances are genuinely thermospheric phenomena or merely artifacts resulting from OH airglow radiation contamination. Notably, thermospheric CGW nos.1 and 2 (top panel of Fig. 4) were unambiguously observed. Their spatial mapping onto OH images confirms these signals originate from the thermosphere (bottom panel of Fig. 4), excluding OH contamination. Regarding the contamination of 630 nm images by OH emissions and the actual propagation situations of CGWs in the thermosphere, please refer to the Supplement (<http://doi.org/10.5446/69989>, Li, 2025b).

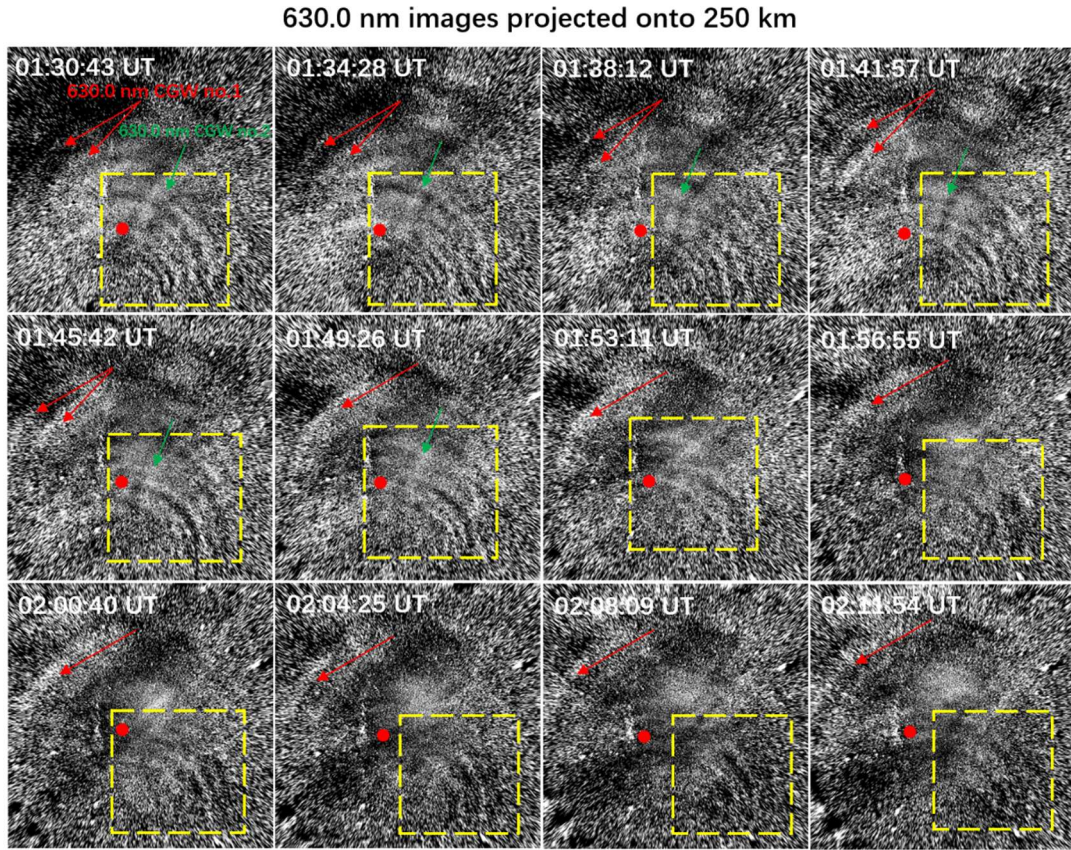


292

293 **Figure 4.** All-sky 630.0 nm images (top panel) and OH images (bottom panel) were both
 294 projected onto an altitude of 87 km with an area of 1000 km \times 1000 km. The northeastward-
 295 propagating CGW (marked with a yellow dashed box) shows contamination from OH airglow
 296 emission. Thermospheric CGWs propagating northwestward confirmed in 630.0 nm images (top
 297 panel). The phase fronts of the thermospheric CGW nos. 1 (red lines) and 2 (green lines) are
 298 superimposed onto the OH images (bottom panel).

299 Figure 5 presents a series of OI 630 nm airglow emission images projected onto
 300 an altitude of 250 km. The ring-shaped arc (thermospheric CGW no. 1) (indicated by
 301 red arrows) propagating towards the northwest was identified, with a wavelength of
 302 approximately 165 km and a horizontal observed phase speed of about 183 ms⁻¹.
 303 There are also observed curved wave structures (thermospheric CGW no. 2)
 304 (indicated by green arrows) whose wave fronts are perpendicular to those of the
 305 contaminating OH wave fronts. The optical signatures of medium-scale traveling
 306 ionospheric disturbances (MSTIDs) in the southern hemisphere, as observed in OI

307 630.0 nm emission images, typically manifest as alternating dark and bright bands
 308 aligned along the northeast-southwest direction, propagating in a northwestward
 309 direction (Candido et al., 2008). The MSTIDs generally exhibit full FOV coverage,
 310 traversing the entire imaging region during their propagation. However, our
 311 observations revealed that the thermospheric disturbances first emerged in the zenith
 312 region, exhibiting distinctively arcuate phase fronts, suggesting that they were excited
 313 by a quasi-point source in the lower atmosphere. The fitted center of the arc (indicated
 314 by a red dot) is located ~ 320 km to the southwest of the station.

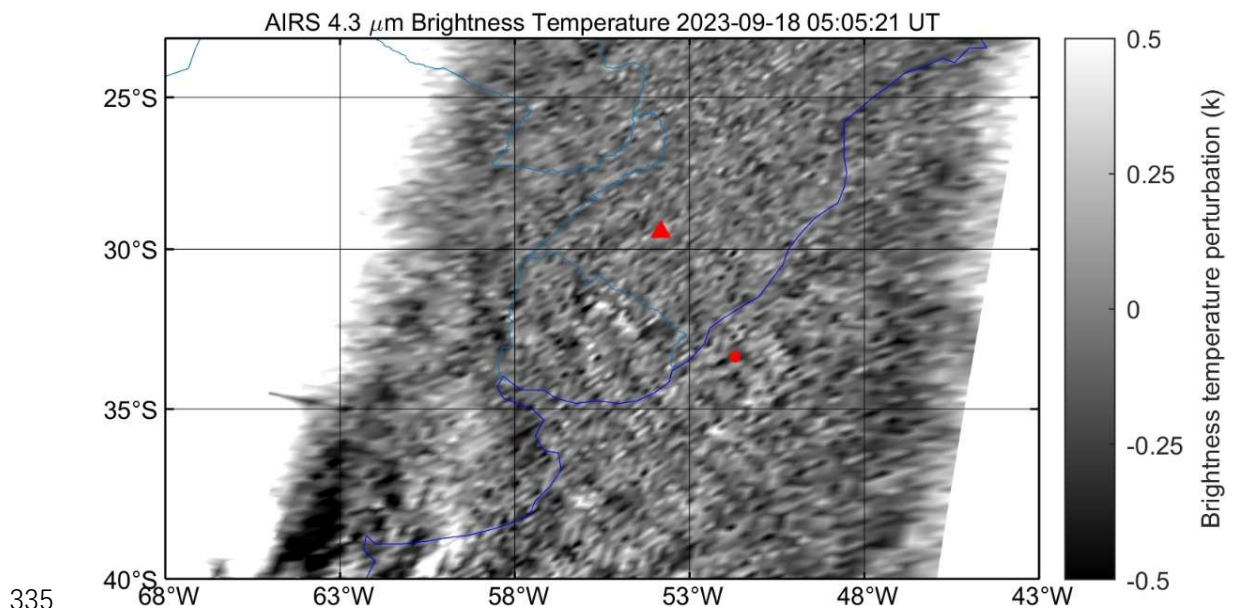


315
 316 **Figure 5.** All-sky 630.0 nm images projected onto an area of $2000 \text{ km} \times 2000 \text{ km}$
 317 showing the thermospheric CGW nos.1 (indicated by red arrows) and 2 (indicated by
 318 green arrows) at approximately 4 min intervals in the SMS station on 18 September
 319 2023. The red dots mark the estimated centers of the thermospheric CGW. The
 320 northeastward-propagating CGW (marked with a yellow dashed box) exhibits

321 artifacts influenced by OH airglow emission.

322 **3.2 AIRS and Suomi NPP**

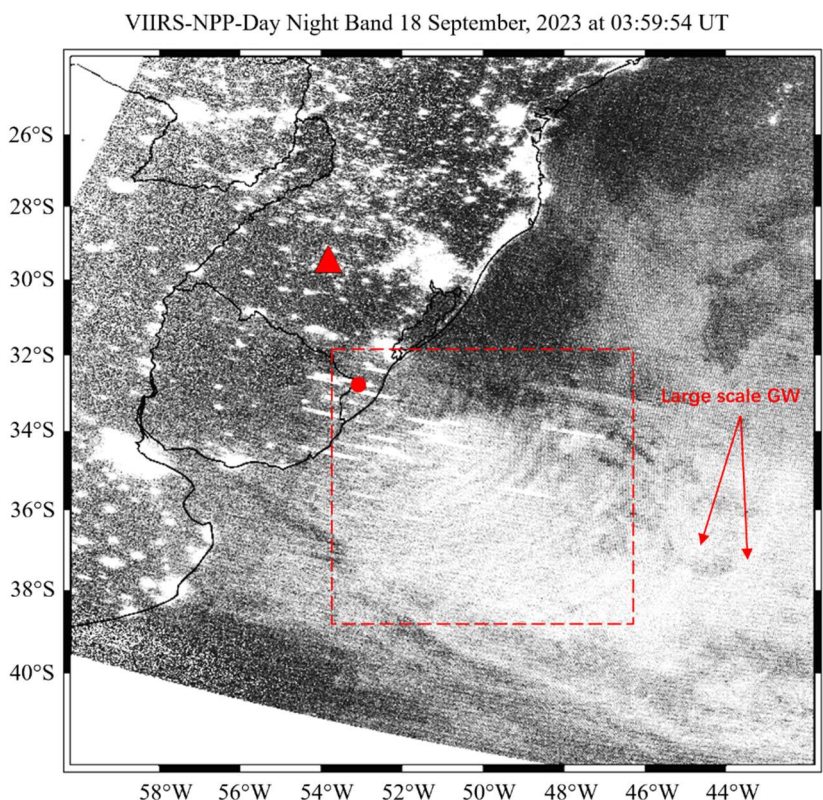
323 Figure 6 shows the AIRS 4.3 μm BT perturbation map over southern Brazil
324 at 05:05:21 UT on 18 September 2023. The AIRS observation reveals large-scale
325 waves propagating northwestward and westward, with a horizontal wavelength of
326 approximately 160 km. The limited spatial resolution of AIRS restricts its
327 detection capability for GWs with short horizontal wavelengths. The relatively
328 weak brightness temperature fluctuations observed by AIRS may result from the
329 instrument's limited sensitivity to short vertical wavelengths (Hoffmann et al., 2014).
330 Consequently, the observed brightness temperature amplitudes are typically much
331 lower than the actual stratospheric temperature fluctuations, especially for convective
332 wave events with short vertical wavelengths. Based on the stratospheric CGW's
333 central position and propagation characteristics, we infer that this wave shares the
334 same source with mesospheric CGW no. 1 identified in the OH all-sky images.



335 **Figure 6.** Aqua satellite 4.3 μm brightness temperature observations of CGWs at 05:05:21 UT on
336 18 September 2023. Brightness temperature is derived from 4.3 μm radiance at an altitude range
337

338 of 30–40 km. The red triangle and dot mark the SMS station and fitted wave center, respectively.

339 The Suomi-NPP satellite flew over Southern Brazil region during the
340 progression of the CGW events. Figure 7 shows CGWs from the S-NPP
341 VIIRS/DNB band measurements at 03:59:54 UT on 18 September 2023. The
342 horizontal wavelengths are primarily distributed within the range of $(38\text{--}52) \pm 3$
343 km (indicated by a red dashed box). In the eastern direction of the small-scale
344 wave region, large-scale waves located at $(34^\circ\text{S}\text{--}39^\circ\text{S}, 43^\circ\text{W}\text{--}46^\circ\text{W})$ were
345 detected with a horizontal wavelength of approximately $154\text{ km} \pm 5\text{ km}$. Due to
346 the interference of urban lighting, the CGW structures were not visible over the
347 land.



348 **Figure 7.** Suomi-NPP satellite Day Night Band radiance observations of CGWs at 03:59:54 UT
349 on 18 September 2023. Red triangle represents the SMS station, and the red dot represents the
350 position of the fitted center of the CGW.
351

3.3 GOES Observations of Convective Plumes

Figure 8 shows GOES-16 10.3 μm BT over southern Brazil from 21:00 UT to 05:30 UT on 17-18 September 2023. The first convective system initially appeared in the southwest direction of the station (indicated by the red arrow) at around 21:00 UT. This convective system continued to move eastward over time and had traveled approximately 400 kilometers by 05:30 UT. This eastward motion explains the observed ~ 436 km displacement of CGW no. 1 in the mesopause region. The second and third convective systems appeared at approximately 02:30 UT and 04:30 UT, respectively, and also moved eastward. By 06:30 UT, the three convective systems had merged together. The detailed evolution process of thunderstorm systems is provided in Supplement (<http://doi.org/10.5446/69993>, Li, 2025c). The spatial proximity of the three CGW centers to the initiation points of the convective systems strongly suggests these systems served as excitation sources for the CGWs detected by the airglow imager.

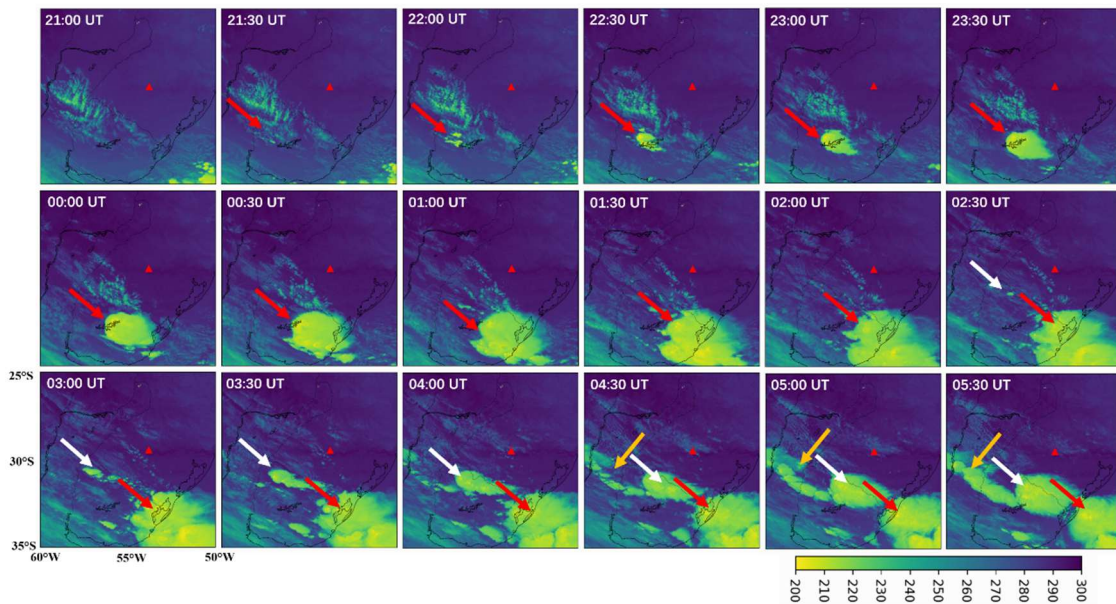


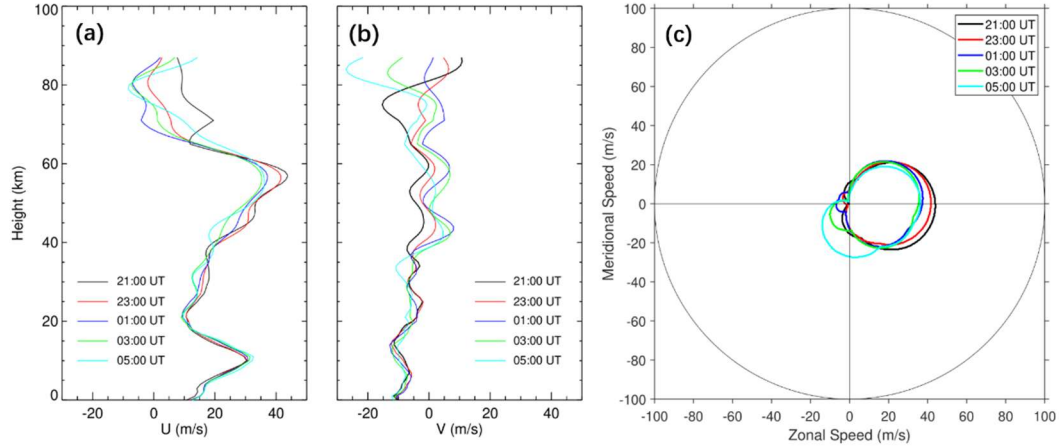
Figure 8. GOES-16 10.3 μm brightness temperature from 21:00 UT to 05:30 UT on 17-18

368 September 2023. The brightness temperature is derived from 10.3 μm infrared radiance data from
369 channel 13. Red triangle represents the SMS station.

370 **4 Results and Discussion**

371 **4.1 The characteristics of mesopause CGWs**

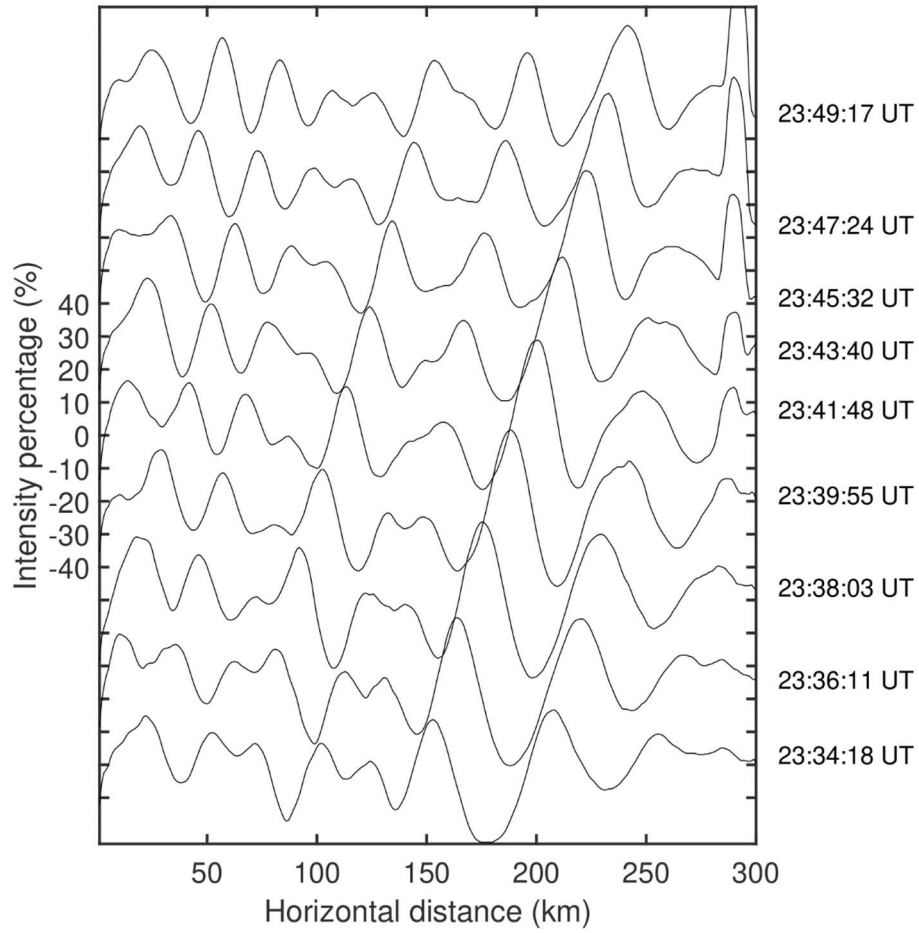
372 We analyzed the background wind field above the station using a composite
373 dataset: the European Centre for Medium-Range Weather Forecasts (ECMWF)
374 ERA5 (Hersbach et al., 2020) for 0-70 km altitude and the Horizontal Wind Model
375 2014 (HWM14; Drob et al., 2015) for 70-87 km altitude. Figure 9a and b show the
376 zonal wind and meridional wind fields, respectively. Figure 9c presents a critical
377 level filtering diagram, demonstrating how gravity waves from the lower atmosphere
378 are prevented from reaching the mesopause region when their phase velocities fall
379 within the prohibited range. The diagram reveals a maximum blocking amplitude of
380 approximately 44 ms^{-1} . The results indicate that weaker background winds
381 (producing smaller blocking amplitudes) enhance the vertical propagation of CGWs
382 from the lower atmosphere to the mesosphere. Apart from the moving convective
383 system mentioned above, which is a primary cause of the eastward displacement of
384 the CGW center observed at the mesopause, the prevailing winds near 10 km and 55
385 km in Fig. 9a also significantly contribute to the eastward movement of the CGW
386 center.



387

388 **Figure 9.** (a) The (a) zonal and (b) meridional wind field profiles from ERA5 (0-70 km) and
 389 HWM14 model (70-87 km) at 21:00 UT, 23:00 UT, 01:00 UT, 03:00 UT, and 05:00 UT,
 390 respectively. (c) Two-dimensional blocking diagrams from 0 to 87 km derived from the wind
 391 profiles in (a) and (b) on 17-18 September 2023.

392 Figure 10 shows sequential cross sections of OH emission intensity
 393 perturbations perpendicular to the CGW no. 1 fronts. The wave amplitudes
 394 observed in this study exhibit significantly stronger perturbations, with a
 395 maximum relative amplitude of 24%. In contrast, previous studies have reported
 396 average amplitudes that are approximately 2% (Li et al., 2016; Tang et al., 2014;
 397 Suzuki et al., 2007a). Additionally, Smith et al. (2020) reported mean-to-peak
 398 wave brightness amplitudes of 10%.

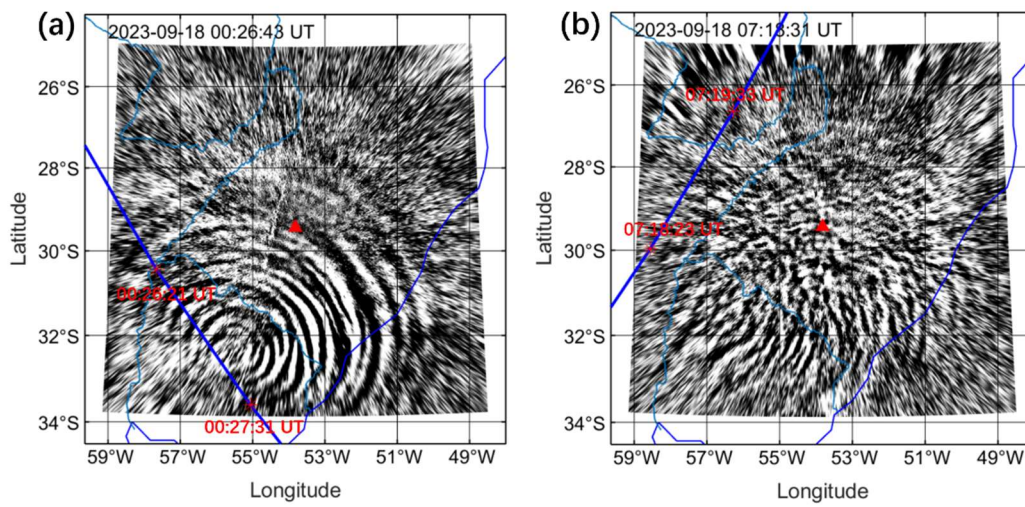


399

400 **Figure 10.** OH emission intensity perturbations perpendicular to the CGW no. 1 fronts (denoted
 401 by the red line in Fig. 2 at 23:39:55 UT) from 23:34:18 UT to 23:49:17 UT on 17-18 September
 402 2023.

403 During the generation and propagation of CGWs, two SABER orbits passed
 404 over the station and happened to be within the field of view of the airglow imager,
 405 as shown in Fig. 11. The first orbit passes over the station at approximately 00:26
 406 UT, followed by a second orbit ~ 7 hours later at 07:18 UT (Fig. 1). Figure 12
 407 presents seven OH airglow emission and temperature profiles from
 408 TIMED/SABER. We observed that the CGWs caused strong disturbances to the
 409 airglow layer. We found that the intensity of airglow emission during the first orbit
 410 (Fig. 12a) was much stronger than that during the second orbit (Fig. 12c), which

411 may suggest that the intensity of the fluctuations during the first orbit was much
 412 stronger than that during the second orbit. In addition to this, we also observed a
 413 double-peaked structure in the airglow emission layer. There are weak double-
 414 peak structures during the first overpass at 00:24:10 UT and 00:28:15 UT. In
 415 contrast, the double-peak structure is more prominent during the second overpass
 416 in the 07:18:23 UT profile.



417
 418 **Figure 11.** Simultaneous observations of mesopause CGWs using OH channel ground-based all-
 419 sky airglow imager and TIMED/SABER satellite measurements. The red triangle marks the
 420 location of the SMS station. The instantaneous field of view of TIMED/SABER is 0.7 mrad by
 421 10 mrad.

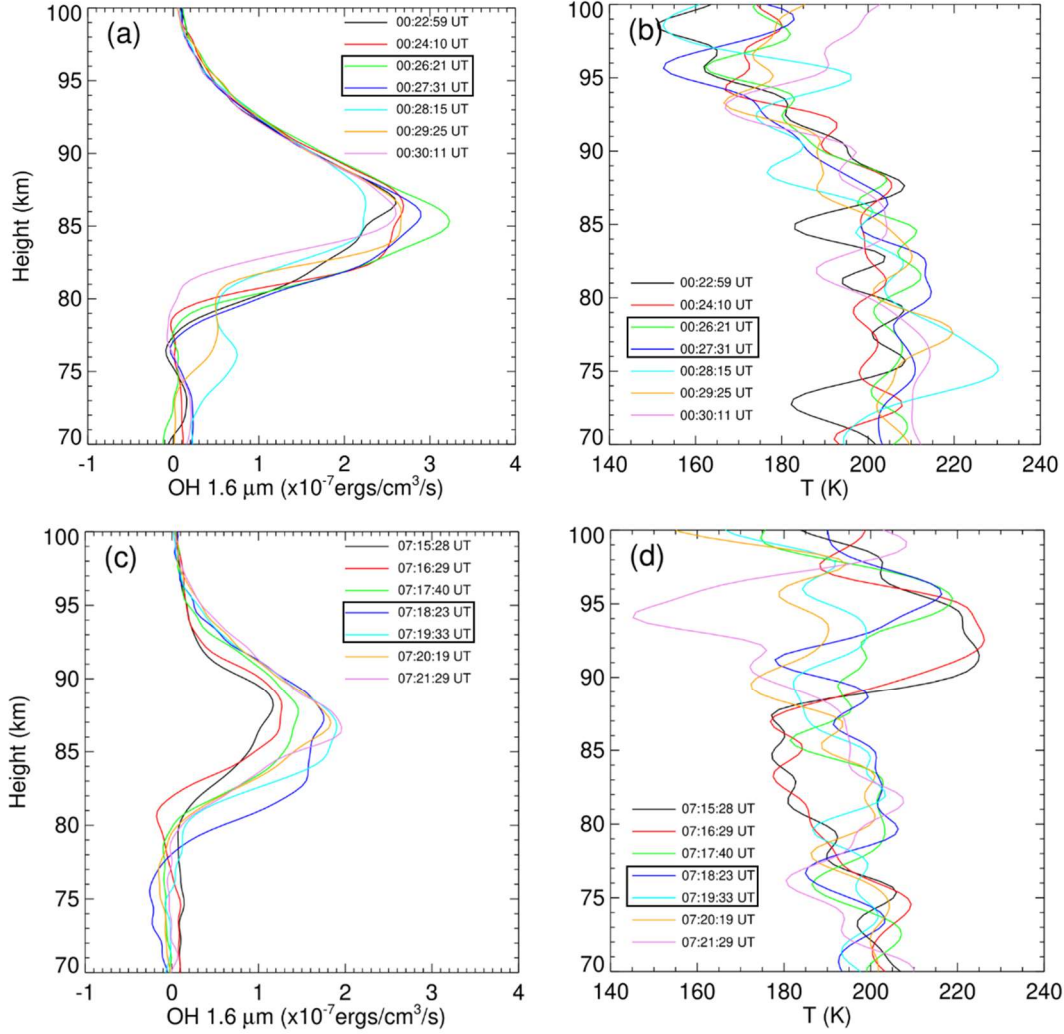


Figure 12. TIMED/SABER (a) OH 1.6 μm emission and (b) temperature profiles (ascending track), and (c) OH 1.6 μm emission and (d) temperature profiles (descending track) on 18 September 2023. Boxed profiles correspond to the satellite's passage through the airglow imager's effective FOV (see Fig. 11).

We can use airglow imaging observations to estimate gravity wave flux (F_M).

The F_M (Swenson and Liu, 1998; Swenson et al., 1999) is expressed as

$$F_M = \frac{1}{2} \frac{g^2}{N^2} \frac{m}{k} \frac{\omega^2}{N^2} \left(\frac{I'}{\bar{I}} \right)^2 \frac{1}{CF^2} (m^2 \cdot s^{-2}), \quad (6)$$

where $CF = 3.5 - (3.5 - 0.1) \exp[-0.0055(\lambda_z - 6\text{km})^2]$ is a cancellation factor. λ_z is the

vertical wavelength. I' is the perturbed airglow intensity. \bar{I} is the averaged airglow

intensity. g is the gravitational acceleration. N is the Brunt-Väisälä frequency

433 derived from TIMED/SABER observations. $k = \frac{2\pi}{\lambda_h}$ is the horizontal wave number.

434 λ_h is the horizontal wavelength derived from airglow images. $\omega = \frac{2\pi c_i}{\lambda_h}$ is the

435 intrinsic frequency (where c_i is the intrinsic phase speed). $m = \frac{2\pi}{\lambda_z}$ is the vertical

436 wave number derived from the GW dispersion relation (Hines, 1960)

$$437 \quad m^2 = \frac{N^2}{(c-u)^2} - k^2 - \frac{1}{4H^2}, \quad (7)$$

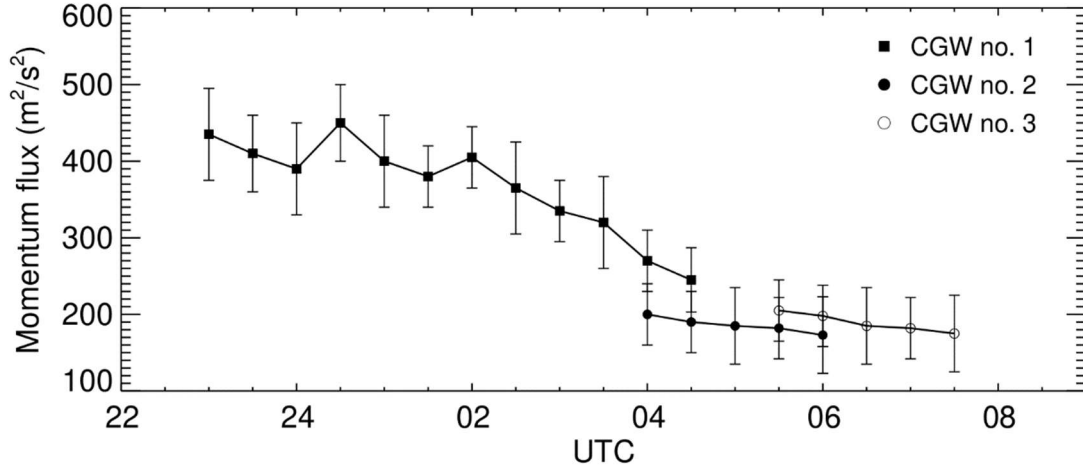
438 where c is the observed horizontal phase speed of the wave, u is the wind speed in the

439 wave direction derived from HWM14, H is the scale height from the SABER

440 temperature profile.

441 Figure 13 shows the calculated vertical flux of the horizontal momentum flux of
442 mesopause CGWs in the altitude of the OH layer from 22:00 to 09:00 UT on 17-18
443 September 2023. We found that CGW no. 1 produced substantially stronger
444 momentum flux (peak value $>450 \text{ m}^2\text{s}^{-2}$) compared to CGW no. 2 and CGW no. 3,
445 which showed similar but weaker magnitudes. These values markedly exceed
446 previous measurements (typically $1\text{--}17 \text{ m}^2\text{s}^{-2}$ in Li et al. 2016 and Tang et al. 2014)
447 and even surpass the intense event (decaying from 300 to $150 \text{ m}^2\text{s}^{-2}$) reported by Smith
448 et al. (2020). Ern et al. (2018) studied the climatology momentum flux determined
449 from SABER satellite limb sounding data. They find that the GW absolute
450 momentum flux is approximately $1\text{--}4 \text{ m}^2\text{s}^{-2}$ in the mesopause region. The results
451 reveal that the fast-moving thunderstorm systems generated exceptionally powerful
452 wave activity, transporting substantial momentum and energy into the MLT region.

453 This demonstrates remarkable wave coupling between the lower and upper
 454 atmosphere.



455
 456 **Figure 13.** Temporal evolution of vertical flux of horizontal momentum from 22:00 to 09:00
 457 UT on 17-18 September 2023.

458 We use the following vertical group velocity equation to estimate the time
 459 required for the CGWs generated by the convective systems to propagate to the MLT
 460 region.

$$461 \quad C_{gz} = \frac{\Delta z}{\Delta t} = -\frac{Nkm}{(k^2 + m^2)^{3/2}}, \quad (8)$$

462 where Δz and Δt are the vertical distance and propagation time of the CGWs from
 463 the troposphere to the airglow layer, respectively. The horizontal wavenumber k is
 464 derived from airglow images. The Brunt-Väisälä frequency N and vertical
 465 wavenumber m were calculated as the mean value over the atmospheric layer
 466 spanning from the tropopause to the mesopause. Notably, the background wind and
 467 temperature may exhibit significant altitudinal variations, resulting in substantial
 468 variations in the CGW vertical group velocity.

469 The background temperature for calculating the vertical group velocity of CGW

no. 1, no. 2, and no. 3 was derived from TIMED/SABER profiles within effective FOV of the OH imager during the first orbit (Fig. 12b), the average of the first and second orbits (Fig. 12d), and the second orbit, respectively, while wind field data combined ERA5 (0–70 km) and HWM14 (70–87 km). The vertical group velocities of CGW no. 1, CGW no. 2, and CGW no. 3 are estimated to be 27–42 ms⁻¹, 21–32 ms⁻¹, and 24–31 ms⁻¹, respectively. This implies that the time taken for CGW no. 1, CGW no. 2, and CGW no. 3 to reach the OH airglow layer (87 km) is approximately 28–44 min, 37–57 min, and 38–50 min, assuming the excitation height of CGWs is 15 km. Yue et al. (2013) conducted multilayer observations of convective gravity waves over the western Great Plains of North America and estimated that the time from the convective source to the airglow layer was ~45 min.

4.2 The characteristics of thermospheric CGWs

We further investigated the propagation characteristics of thermospheric CGW no. 1. The vertical group velocity of the thermospheric gravity waves can be estimated using the following approximate relationship: $C_{gz} \sim -\frac{N}{k} \cos^2 \alpha \sin \alpha$. α is zenith angle between the vertical altitude and propagation direction of the CGWs phase fronts. The zenith angle α is approximately 61° from Fig. 14a. The buoyancy frequency N is estimated to be $2\pi/10.35$ min at the thermosphere height of 250 km, which is derived from the empirical neutral atmosphere model (NRLMSISE-00) (Picone et al., 2002). The horizontal wavenumber $k=2\pi/165$ km. The estimated vertical group velocity is about 54 ± 6 ms⁻¹. Based on the vertical group velocity, we find that the time taken for the gravity waves to propagate from the OH layer and the

492 tropopause region to the thermosphere is approximately 50 ± 5 min and 73 ± 8 min,
493 respectively. As discussed above, the OH images and OI images were captured nearly
494 simultaneously to illustrate the contamination effect in Fig. 4. Some of the wave
495 pattern mismatches in Fig. 4 are due to the propagation time required for CGWs to
496 travel from the OH altitude to the OI altitude. Given the thermospheric arrival time
497 of 01:41:57 UT (Fig. 14a), the CGWs were likely excited near the tropopause (~ 15
498 km altitude) at approximately 00:28:57 UT (Fig. 14c), passed through the OH layer
499 (~ 87 km altitude) between approximately 00:46:57 UT and 00:56:57 UT. Notably,
500 GWs with comparable scales were observed in the OH layer at around 00:54:48 UT
501 (Fig. 14b), which suggests that they might be the same wave.

502 As mentioned above, the observed thermospheric CGWs exhibits an asymmetric
503 structure, appearing as arc-shaped waves only in the western and northwestern
504 directions. This asymmetry can be attributed to the Doppler effect of the background
505 wind field, which influences gravity wave detection through wave cancellation. GWs
506 propagating against background wind are Doppler shifted to a larger vertical
507 wavelength, and increased chance of observation (Li et al., 2016). These GWs suffer
508 little cancelation and can be easily detected by airglow imager GWs observations.
509 GWs propagating along background wind are Doppler shifted to a smaller vertical
510 wavelength, causing the wave amplitude to become invisible. As illustrated in Fig.
511 14d, the eastward zonal wind at 250 km altitude reaches ~ 90 ms^{-1} . This strong
512 eastward wind likely suppresses the visibility of eastward-propagating thermospheric
513 CGWs in airglow imaging. We use Eq. 5 to estimate that the vertical wavelength of

thermospheric CGWs propagating in the northwest direction is approximately 236 km, while that of thermospheric CGWs propagating eastward is approximately 62 km. The Doppler shift reduces their vertical wavelengths, causing them to fall below the detection threshold of the vertically integrated airglow observations, which is approximately 100 km from 200 km to 300 km during nighttime (Chiang et al., 2018).

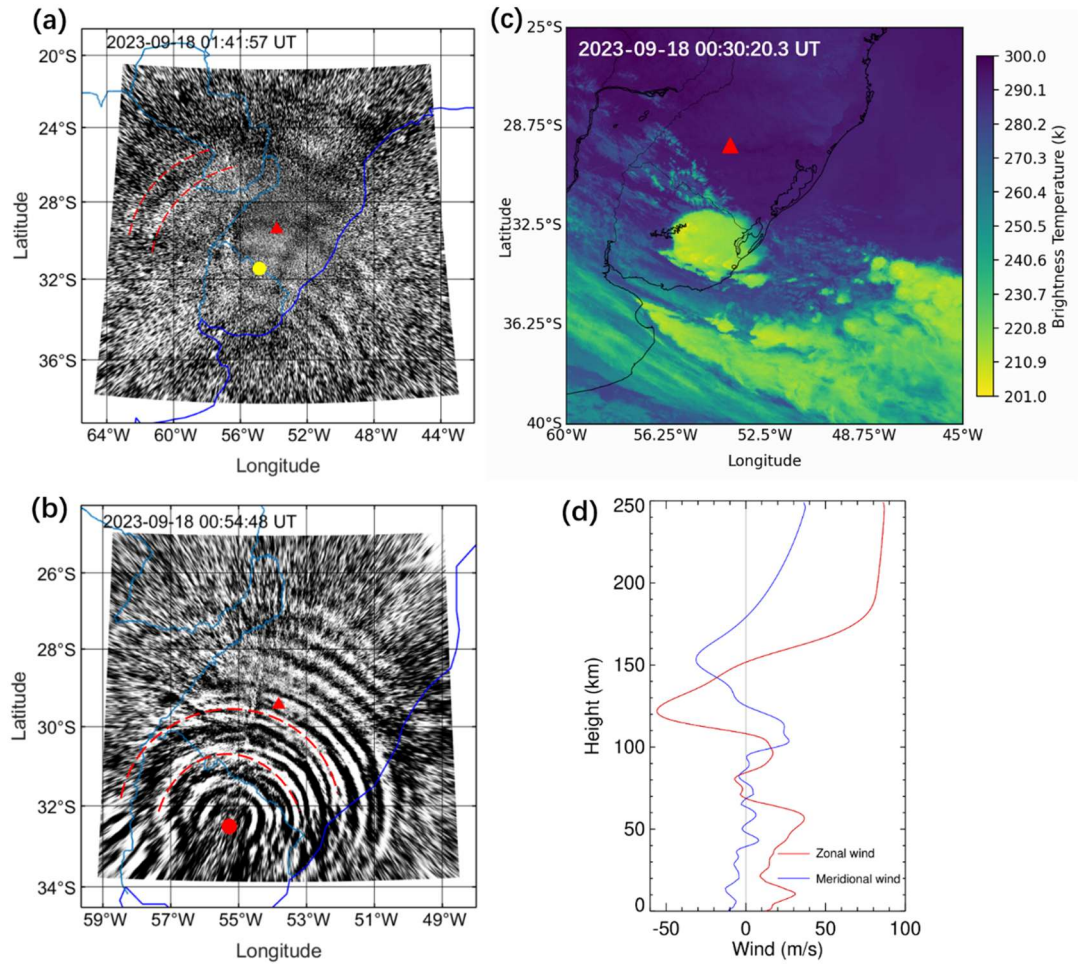


Figure 14. (a) All-sky 630.0 nm imaging observation of thermospheric CGW (red dashed lines) at 01:41:57 UT on 18 September 2023. The yellow dot marks the estimated center of the thermospheric CGW. (b) All-sky OH imaging observation of mesospheric CGW at 00:54:48 UT on 18 September 2023. The red dashed lines mark out the mesospheric CGW with the same scale as the thermospheric CGW. The red dot marks the estimated center of the mesospheric CGW. (c) GOES-16 10.3 μm brightness temperature at 00:20:20 UT on 17-18 September 2023. The red triangle marks the location of the SMS station. (d) Wind profiles from ERA-5 (0-70 km) and

527 HWM14 (70-250 km) averaged between 01:00 UT and 02:00 UT on 18 September 2023.

528 **5 Conclusions**

529 In this study, we investigated intense CGWs using coordinated dual-channel
530 airglow observations (630.0 nm and OH bands) from the Southern Space Observatory
531 (SSO) in São Martinho da Serra, Brazil, complemented by multi-satellite
532 measurements during 17-18 September 2023. The key findings are summarized as
533 follows:

534 These unprecedented CGWs exhibited remarkable persistence (>10 hours),
535 extreme amplitude perturbations ($>24\%$), and substantial wave-center movement
536 (>400 km). These wave events were unambiguously linked to fast-moving
537 convective systems observed by GOES-16. The weaker background wind field
538 during the spring season transition was identified as a crucial factor that allowed
539 CGWs to propagate from the lower atmosphere to the MLT region.

540 The OI 630 nm airglow observations were substantially contaminated by
541 overlapping OH Meinel band emissions (715-930 nm). This contamination leads
542 to spurious apparent vertical coupling, as mesospheric gravity waves (CGWs) are
543 artificially projected onto the thermospheric OI 630 nm emission layer. This cross-
544 layer aliasing effect necessitates rigorous validation protocols when interpreting
545 putative thermospheric disturbances at 630 nm, particularly requiring spatio-
546 temporally collocated OH airglow measurements (e.g., OH (9–3) bands) to
547 discriminate genuine dynamical processes from lower atmospheric contamination
548 artifacts.

549 The asymmetric propagation of CGWs in the thermosphere was attributed to
550 variations in vertical wavelength induced by the Doppler effect of background winds.
551 Specifically, the eastward zonal wind at 250 km altitude, reaching approximately 90
552 ms^{-1} , reduced the vertical wavelength of eastward-propagating CGWs, making them
553 undetectable in airglow imaging observations due to vertical integration effects.

554 This study reveals intense CGWs originating from deep convective systems that
555 play a dominant role in transferring wave energy and momentum from the
556 troposphere to the MLT region. These waves exhibited exceptional characteristics
557 including prolonged persistence, extreme amplitude perturbations, and significant
558 horizontal movement, demonstrating their substantial impact on atmospheric
559 dynamics and space weather by (1) seeding traveling ionospheric disturbances (TIDs)
560 that disrupt communications/GPS, (2) triggering plasma instabilities, and (3) altering
561 thermospheric density, affecting satellite drag.

562 Our coordinated multi-instrument approach, combining dual-channel airglow
563 observations with satellite measurements, provides crucial insights into wave
564 propagation while addressing the challenges of cross-layer contamination in OI 630
565 nm emissions. These findings significantly advance our understanding of gravity
566 wave dynamics in the upper atmosphere and establish an improved observational
567 framework for studying atmospheric coupling processes.

568

569 **Data availability.** The airglow data are available from the web page of the Estudo e
570 Monitoramento Brasileiro do Clima Espacial (EMBRACE/INPE) at

571 <http://www2.inpe.br/climaespacial/portal/en> (EMBRACE, 2024). TIMED/SABER
 572 data are accessible from <http://saber.gats-inc.com/data.php> (Mlynczak et al., 2023).
 573 The ERA5 reanalysis data are available for download from the Copernicus Climate
 574 Change Service Climate Data Store at <https://doi.org/10.24381/cds.bd0915c6>
 575 (Hersbach et al., 2023). The GOES-16 ABI L1b radiances data are accessible from
 576 <https://www.ncdc.noaa.gov/airs-web/search> (Schmit et al., 2017). AIRS radiance
 577 data are accessible from https://disc.gsfc.nasa.gov/datasets/AIRIBRAD_005/
 578 summary (AIRS project, 2007). VIIRS DNB data are distributed by the NOAA
 579 Comprehensive Large Array-data Stewardship System
 580 (CLASS)([https://www.aev.class.noaa.gov/saa/products/welcome;jsessionid=C3562F](https://www.aev.class.noaa.gov/saa/products/welcome;jsessionid=C3562F228661BE845B176C9AE2714AE6)
 581 [228661BE845B176C9AE2714AE6](https://www.aev.class.noaa.gov/saa/products/welcome;jsessionid=C3562F228661BE845B176C9AE2714AE6)) (Miller et al., 2012).

582

583 **Video supplement.** Extreme mesospheric concentric gravity waves from OH
 584 airglow observations over Southern Brazil is available for view
 585 (<http://doi.org/10.5446/69990>, Li, 2025a). Thermospheric concentric gravity
 586 waves from OI 630 nm airglow observations over Southern Brazil is available for
 587 view (<http://doi.org/10.5446/69989>, Li, 2025b). Fast-moving severe thunderstorms
 588 over Southern Brazil from GOES-16 observations is available for view
 589 (<http://doi.org/10.5446/69993>, Li, 2025c).

590

591 **Author contributions.** QL conceived the idea of the article and wrote the manuscript.
 592 JX carried out the analysis of the AIRS and NPP data. XL contributed to the analysis

593 of the SABER data. YZ contributed to the processing of ECMWF data. WY, XL, HL,
594 and ZL contributed to the data interpretation and manuscript preparation. CMW and
595 JVB revised the manuscript. All authors discussed the results and commented on the
596 paper.

597
598 **Competing interests.** The contact author has declared that none of the authors has
599 any competing interests.

600
601 **Acknowledgements.** We thank the National Natural Science Foundation of China
602 (grant nos. 42374205). The authors thank the Estudo e Monitoramento Brasileiro do
603 Clima Espacial (EMBRACE/INPE) for the provision of the all-sky data. We
604 acknowledge the use of data from the Chinese Meridian Project. We appreciate the
605 TIMED/SABER team for providing the temperature and emission intensity data. We
606 also thank the European Centre for Medium-Range Weather Forecasts (ECMWF) for
607 the provision of the ERA5 data and Geostationary Operational Environmental
608 Satellite (GOES) team for the ABI L1b radiances data. We also thank the NASA
609 Goddard Earth Sciences Data Information and Services Center (GES DISC) for
610 providing AIRS data and NOAA Comprehensive Large Array-data Stewardship
611 System (CLASS) for providing Day Night Band data.

612

613 **Financial support.** This research has been supported by the National Natural Science
614 Foundation of China (grant nos. 42374205) and the Specialized Research Fund of
615 National Space Science Center, Chinese Academy of Sciences (grant no. E4PD3010).
616 This work has been supported by the B-type Strategic Priority Program of CAS (grant
617 no. XDB0780000) and China-Brazil Joint Laboratory for Space Weather (No.
618 119GJHZ2024027MI). The project has also been supported by the Specialized
619 Research Fund for State Key Laboratories.

References

- AIRS project: AIRS/Aqua L1B Infrared (IR) geolocated and calibrated radiances V005, Greenbelt, MD, USA, Goddard Earth Sciences Data and Information Services Center (GES DISC), [data set], <https://doi.org/10.5067/YZEXEVN4JGGJ>, 2007.
- Alexander, M. J., and Holton, J. R.: On the spectrum of vertically propagating gravity waves generated by a transient heat source, *Atmos. Chem. Phys.*, 4, 923–932, <https://doi.org/10.5194/acp-4-923-2004>, 2004.
- Aumann, H. H., Chahine, M. T., Gautier, C., Goldberg, M. D., Kalnay, E., McMillin, L. M., Revercomb, H., Rosenkranz, P. W., Smith, W. L., Staelin, D. H., Strow, L. L., and Susskind, J.: AIRS/AMSU/HSB on the aqua mission: Design, science objectives, data products, and processing systems, *IEEE T. Geosci. Remote Sens.*, 41, 253–264, <https://doi.org/10.1109/TGRS.2002.808356>, 2003.
- Burnside, R. G., Meriwether, J. W., and Torr, M. R.: Contamination of ground-based measurements of OI (6300 Å) and NI (5200 Å) airglow by OH emissions, *Planet. Space. Sci.*, 25(10), 985–988, [https://doi.org/10.1016/0032-0633\(77\)90012-5](https://doi.org/10.1016/0032-0633(77)90012-5), 1977.
- Candido, C. M. N., Pimenta, A. A., Bittencourt, J. A., and Becker-Guedes, F.: Statistical analysis of the occurrence of medium-scale traveling ionospheric disturbances over Brazilian low latitudes using OI 630.0 nm emission all-sky images, *Geophys. Res. Lett.*, 35, L17105,

642 <https://doi.org/10.1029/2008GL035043>, 2008.

643 Cao, B., and Liu, A. Z.: Intermittency of gravity wave momentum flux in the
644 mesopause region observed with an all-sky airglow imager, *J. Geophys. Res.*
645 *Atmos.*, 121, <https://doi.org/10.1002/2015JD023802>, 2016.

646 Chahine, M. T., Pagano, T. S., Aumann, H. H., Atlas, R., Barnet, C., Blaisdell, J.,
647 Chen, L., Divakarla, M., Fetzer, E. J., Goldberg, M., Gautier, C.,
648 Granger, S., Hannon, S., Irion, F. W., Kakar, R., Kalnay, E.,
649 Lambrigtsen, B. H., Lee, S.-Y., Marshall, J. L., Mcmillan, W. W.,
650 Mcmillin, L., Olsen, E. T., Revercomb, H., Rosenkranz, P., Smith, W. L.,
651 Staelin, D., Strow, L. L., Susskind, J., Tobin, D., Wolf, W., and Zhou, L.:
652 AIRS, *B. Am. Meteorol. Soc.*, 87, 911–926, [https://doi.org/10.1175/bams-](https://doi.org/10.1175/bams-87-7-911)
653 87-7-911, 2006.

654 Chiang, C.-Y., Tam, S. W.-Y., and Chang, T.-F.: Variations of the 630.0 nm
655 airglow emission with meridional neutral wind and neutral temperature
656 around midnight, *Ann. Geophys.*, 36, 1471–1481,
657 <https://doi.org/10.5194/angeo-36-1471-2018>, 2018.

658 Dalin, P., Gavrilov, N., Pertsev, N., Perminov, V., Pogoreltsev, A., Shevchuk, N.,
659 Dubietis, A., Völger, P., Zalcik, M., Ling, A., Kulikov, S., Zadorozhny, A.,
660 Salakhutdinov, G., and Grigoryeva, I.: A case study of long gravity wave
661 crests in noctilucent clouds and their origin in the upper tropospheric jet
662 stream, *J. Geophys. Res.-Atmos.*, 121, 14102–14116,
663 <https://doi.org/10.1002/2016JD025422>, 2016.

664 Dalin, P., Brändström, U., Kero, J., Voelger, P., Nishiyama, T., Trondsen, T.,
 665 Wyatt, D., Unick, C., Perminov, V., Pertsev, N., and Hedin, J.: A novel
 666 infrared imager for studies of hydroxyl and oxygen nightglow emissions in
 667 the mesopause above northern Scandinavia, *Atmos. Meas. Tech.*, 17, 1561–
 668 1576, <https://doi.org/10.5194/amt-17-1561-2024>, 2024.

669 Drob, D. P., Emmert, J. T., Meriwether, J. W., Makela, J. J., Doornbos, E., Conde,
 670 M., Hernandez, G., Noto, J., Zawdie, K. A., McDonald, S. E., Huba, J. D.,
 671 and Klenzing, J. H.: An update to the Horizontal Wind Model (HWM): The
 672 quiet time thermosphere, *Earth and Space Science*, 2, 301–319,
 673 <https://doi.org/10.1002/2014EA000089>, 2015.

674 EMBRACE: Estudo e Monitoramento Brasileiro do Clima Espacial–
 675 EMBRACE/INPE, <http://www2.inpe.br/climaespacial/portal/en> (last
 676 access: 15 September 2024), 2024.

677 Ern, M., Trinh, Q. T., Preusse, P., Gille, J. C., Mlynchak, M. G., Russell III, J. M.,
 678 and Riese, M.: GRACILE: a comprehensive climatology of atmospheric
 679 gravity wave parameters based on satellite limb soundings, *Earth Syst. Sci.*
 680 *Data*, 10, 857–892, <https://doi.org/10.5194/essd-10-857-2018>, 2018.

681 Ern, M., Hoffmann, L., Rhode, S., and Preusse, P.: The mesoscale gravity wave
 682 response to the 2022 Tonga volcanic eruption: AIRS and MLS satellite
 683 observations and source backtracing, *Geophysical Research Letters*, 49,
 684 e2022GL098626, <https://doi.org/10.1029/2022GL098626>, 2022

685 Ern, M., Preusse, P., and Riese, M.: Intermittency of gravity wave potential

686 energies and absolute momentum fluxes derived from infrared limb
 687 sounding satellite observations, *Atmos. Chem. Phys.*, 22, 15093–15133,
 688 <https://doi.org/10.5194/acp-22-15093-2022>, 2022.

689 Fovell, R., Durran, D., and Holton, J. R.: Numerical simulations of convectively
 690 generated stratospheric gravity waves, *J. Atmos. Sci.*, 49, 1427–1442,
 691 [https://doi.org/10.1175/15200469\(1992\)049<1427:NSOCGS>2.0.CO;2](https://doi.org/10.1175/15200469(1992)049<1427:NSOCGS>2.0.CO;2)
 692 92.

693 Franco-Diaz, E., Gerding, M., Holt, L., Strelnikova, I., Wing, R., Baumgarten,
 694 G., and Lübken, F.-J.: Convective gravity wave events during summer near
 695 54° N, present in both AIRS and Rayleigh–Mie–Raman (RMR) lidar
 696 observations, *Atmos. Chem. Phys.*, 24, 1543–1558,
 697 <https://doi.org/10.5194/acp-24-1543-2024>, 2024.

698 Fritts, D. C.: Shear excitation of atmospheric gravity waves, *J. Atmos. Sci.*, 39,
 699 1936–1952, [https://doi.org/10.1175/1520-0469\(1982\)039<1936:SEOAGW>](https://doi.org/10.1175/1520-0469(1982)039<1936:SEOAGW>2.0.CO;2)
 700 2.0.CO;2, 1982.

701 Fritts, D. C., and Alexander, M. J.: Gravity wave dynamics and effects in the
 702 middle atmosphere, *Reviews of Geophysics*, 41(1), [https://doi.](https://doi.org/10.1029/2001RG000106)
 703 [org/10.1029/2001RG000106](https://doi.org/10.1029/2001RG000106), 2003.

704 Fritts, D. C., and Nastrom, G. D.: Sources of Mesoscale Variability of Gravity
 705 Waves. Part II: Frontal, Convective, and Jet Stream Excitation, *Journal of*
 706 *the Atmospheric Sciences* 49, 111–127, [https://doi.org/10.1175/1520-](https://doi.org/10.1175/1520-0469(1992)049<0111:SOMVOG>2.0.CO;2)
 707 [0469\(1992\)049<0111:SOMVOG>2.0.CO;2](https://doi.org/10.1175/1520-0469(1992)049<0111:SOMVOG>2.0.CO;2), 1992.

708 Garcia, F. J., Taylor, M. J., and Kelley, M. C.: Two-dimensional spectral analysis
 709 of mesospheric airglow image data, *Appl. Optics*, 36, 7374 – 7385,
 710 <https://doi.org/10.1364/AO.36.007374>, 1997. Geldenhuys, M., Preusse, P.,
 711 Krisch, I., Zülicke, C., Ungermann, J., Ern, M., Friedl-Vallon, F., and Riese,
 712 M.: Orographically induced spontaneous imbalance within the jet causing a
 713 large-scale gravity wave event, *Atmos. Chem. Phys.*, 21, 10393–10412,
 714 <https://doi.org/10.5194/acp-21-10393-2021>, 2021.

715 Hapgood, M. and Taylor, M. J.: Analysis of airglow image data, *Ann. Geophys.*,
 716 38, 805–813, 1982.

717 Heale, C. J., Bossert, K., Vadas, S. L., Hoffmann, L., Dornbrack, A., Stober, G.,
 718 Snively, J. B., and Jacobi, C.: Secondary gravity waves generated by
 719 breaking mountain waves over Europe, *J. Geophys. Res.-Atmos.*, 125,
 720 e2019JD031662, <https://doi.org/10.1029/2019JD031662>, 2020.

721 Heale, C. J., Inchin, P. A., and Snively, J. B.: Primary Versus Secondary Gravity
 722 Wave Responses at F-Region Heights Generated by a Convective Source, *J.*
 723 *Geophys. Res.-Space*, 127, e2021JA029947, [https://doi.org/10.1029/](https://doi.org/10.1029/2021JA029947)
 724 [2021JA029947](https://doi.org/10.1029/2021JA029947), 2022.

725 Hernandez, G.: Contamination of the OI (3 P₂–1 D₂) emission line by the (9–3)
 726 band of OH X₂ II in high-resolution measurements of the night sky, *J.*
 727 *Geophys. Res.*, 79, 1119–1123, <https://doi.org/10.1029/JA079i007p01119>,
 728 1974.

729 Hersbach, H., Bell, B., Berrisford, P., Hirahara, S., Horányi, A., Muñoz-Sabater,

730 J., Nicolas, J., Peubey, C., Radu, R., Schepers, D., Simmons, A., Soci, C.,
 731 Abdalla, S., Abellan, X., Balsamo, G., Bechtold, P., Biavati, G., Bidlot, J.,
 732 Bonavita, M., De Chiara, G., Dahlgren, P., Dee, D., Diamantakis, M.,
 733 Dragani, R., Flemming, J., Forbes, R., Fuentes, M., Geer, A., Haimberger,
 734 L., Healy, S., Hogan, R. J., Hólm, E., Janisková, M., Keeley, S., Laloyaux,
 735 P., Lopez, P., Lupu, C., Radnoti, G., deRosnay, P., Rozum, I., Vamborg, F.,
 736 Villaume, S., and Thépaut, J. N.: The ERA5 global reanalysis, Q. J. Roy.
 737 Meteor. Soc., 146, 1999–2049, <https://doi.org/10.1002/qj.3803>, 2020.
 738 Hersbach, H., Bell, B., Berrisford, P., Biavati, G., Horányi, A., Muñoz Sabater,
 739 J., Nicolas, J., Peubey, C., Radu, R., Rozum, I., Schepers, D., Simmons, A.,
 740 Soci, C., Dee, D., and Thépaut, J.- N.: ERA5 hourly data on pressure levels
 741 from 1940 to present, Copernicus Climate Change Service (C3S) Climate
 742 Data Store (CDS) [data set], <https://doi.org/10.24381/cds.bd0915c6>, 2023.
 743 Hines, C. O.: Internal atmospheric gravity waves at ionospheric heights. Can. J.
 744 Phys., 38(11), 1441–1481, <https://doi.org/10.1139/p60-150>, 1960.
 745 Hoffmann, L., and Alexander, M. J.: Occurrence frequency of convective gravity
 746 waves during the North American thunderstorm season, J. Geophys. Res.,
 747 115, D20111, <https://doi.org/10.1029/2010JD014401>, 2010.
 748 Hoffmann, L., Alexander, M. J., Clerbaux, C., Grimsdell, A. W., Meyer, C. I.,
 749 Rößler, T., and Tournier, B.: Intercomparison of stratospheric gravity wave
 750 observations with AIRS and IASI, Atmos. Meas. Tech., 7, 4517–4537,
 751 <https://doi.org/10.5194/amt-7-4517-2014>, 2014.

752 Inchin, P. A., Bhatt, A., Bramberger, M., Chakraborty, S., Debchoudhury, S., and
 753 Heale, C.: Atmospheric and ionospheric responses to orographic gravity
 754 waves prior to the December 2022 cold air outbreak, *Journal of Geophysical*
 755 *Research: Space Physics*, 129, e2024JA032485. [https://doi.org/10.1029/](https://doi.org/10.1029/2024JA032485)
 756 2024JA032485, 2024.

757 Kubota, M., Fukunishi, H., and Okano, S.: Characteristics of medium-and large-
 758 scale TIDs over Japan derived from OI 630- nm nightglow observation,
 759 *Earth Planets Space*, 53, 741–751. <https://doi.org/10.1186/BF03352402>,
 760 2001.

761 Lane, T. P., Reeder, M. J., and Clark, T. L.: Numerical modeling of gravity wave
 762 generation by deep tropical convection, *J. Atmos. Sci.*, 58, 1249–1274,
 763 [https://doi.org/10.1175/1520-0469\(2001\)0582.0.CO;2](https://doi.org/10.1175/1520-0469(2001)0582.0.CO;2), 2001.

764 Lee, T. F., Nelson, S. C., Dills, P., Riishojgaard, L. P., Jones, A., Li, L., Miller, S.,
 765 Flynn, L. E., Jedlovec, G., McCarty, W, Hoffman, C., and McWilliams, G.:
 766 NPOESS: Next-generation operational global Earth observations, *Bull. Am.*
 767 *Meteorol. Soc.*, 91, 727–740, <https://doi.org/10.1175/2009BAMS2953.1>,
 768 2010.

769 Lewis, J. M., Martin, D. W., Rabin, R. M. and Moosmüller, H.: Suomi: Pragmatic
 770 visionary, *Bull. Am. Meteorol. Soc.*, 91, 559–577, [https://doi.org/10.1175/](https://doi.org/10.1175/2009BAMS2897.1)
 771 2009BAMS2897.1, 2010.

772 Li, Q., Xu, J., Liu, X., Yuan, W., and Chen, J.: Characteristics of mesospheric
 773 gravity waves over the southeastern Tibetan Plateau region, *Journal of*

774 Geophysical Research: Space Physics, 121(9), 9204–9221,
 775 <https://doi.org/10.1002/2016JA022823>, 2016.

776 Li, Q., Xu, J., Gusman, A. R., Liu, H., Yuan, W., Liu, W., Zhu, Y., and Liu, X.:
 777 Upper-atmosphere responses to the 2022 Hunga Tonga–Hunga Ha’apai
 778 volcanic eruption via acoustic gravity waves and air–sea interaction, *Atmos.*
 779 *Chem. Phys.*, 24, 8343–8361, <https://doi.org/10.5194/acp-24-8343-2024>,
 780 2024.

781 Li, Q.: Extreme mesospheric concentric gravity waves from OH airglow
 782 observations over Southern Brazil, TIB AV-Portal [video],
 783 <http://doi.org/10.5446/69990>, 2025a.

784 Li, Q.: Thermospheric concentric gravity waves from OI 630 nm airglow
 785 observations over Southern Brazil, TIB AV-Portal [video],
 786 <http://doi.org/10.5446/69990>, 2025b.

787 Li, Q.: Fast-moving severe thunderstorms over Southern Brazil from GOES-16
 788 observations, TIB AV-Portal [video], <https://doi.org/10.5446/69993>, 2025c.

789 Li, Z., Liu, A. Z., Lu, X., Swenson, G. R., and Franke, S. J.: Gravity wave
 790 characteristics from OH airglow imager over Maui, *J. Geophys. Res.*, 116,
 791 D22115, <https://doi.org/10.1029/2011JD015870>, 2011.

792 Liu, X., Xu, J. Y., Yue, J., Vadas, S. L., and Becker, E.: Orographic primary and
 793 309 secondary gravity waves in the middle atmosphere from 16-year
 794 SABER 310 observations, *Geophysical Research Letters*, 46, 4512–4522,
 795 <https://doi.org/10.1029/2019GL082256>, 2019.

796 Miller, S. D., Mills, S. P., Elvidge, C. D., Lindsey, D. T., Lee, T. F., and Hawkins,
 797 J. D.: Suomi satellite brings to light a unique frontier of nighttime
 798 environmental sensing capabilities, *Proc. Natl. Acad. Sci. U.S.A.*, 109(39),
 799 15,706–15,711, <https://doi.org/10.1073/pnas.1207034109>, 2012 (data
 800 available at [https://www.aev.class.noaa.gov/saa/products/welcome;](https://www.aev.class.noaa.gov/saa/products/welcome;jsessionid=C3562F228661BE845B176C9AE2714AE6)
 801 [jsessionid=C3562F228661BE845B176C9AE2714AE6](https://www.aev.class.noaa.gov/saa/products/welcome;jsessionid=C3562F228661BE845B176C9AE2714AE6), last access: 15
 802 December 2024).
 803 Mlynczak, M. G., Marshall, B. T., Garcia, R. R., Hunt, L., Yue, J., Harvey, V. L.,
 804 Lopez-Puertas, M., Mertens, C., and Russell, J.: Algorithm stability and the
 805 long-term geospace data record from TIMED/SABER, *Geophys. Res. Lett.*,
 806 50, 1–7, <https://doi.org/10.1029/2022GL102398>, 2023 (data available at
 807 <http://saber.gats-inc.com/data.php>, last access: 10 December 2024).
 808 Nastrom, G. D., and Fritts, D. C.: Sources of Mesoscale Variability of Gravity
 809 Waves. Part I: Topographic Excitation, *Journal of the Atmospheric Sciences*
 810 49, 101–110, [https://doi.org/10.1175/1520-0469\(1992\)049<0101:](https://doi.org/10.1175/1520-0469(1992)049<0101:SOMVOG>2.0.CO;2)
 811 [SOMVOG>2.0.CO;2](https://doi.org/10.1175/1520-0469(1992)049<0101:SOMVOG>2.0.CO;2), 1992.
 812 Nyassor, P. K., Wrasse, C. M., Gobbi, D., Paulino, I., Vadas, S. L., Naccarato, K.
 813 P., Takahashi, H., Bageston, J. V., Figueiredo, C. A. O. B., and Barros, D.:
 814 Case Studies on Concentric Gravity Waves Source Using Lightning Flash
 815 Rate, Brightness Temperature and Backward Ray Tracing at São Martinho
 816 da Serra (29.44° S, 53.82° W), *J. Geophys. Res.-Atmos.*, 126,
 817 e2020JD034527, <https://doi.org/10.1029/2020JD034527>, 2021.

818 Nyassor, P. K., Wrasse, C. M., Paulino, I., São Sabbas, E. F. M. T., Bageston, J.
 819 V., Naccarato, K. P., Gobbi, D., Figueiredo, C. A. O. B., Ayorinde, T. T.,
 820 Takahashi, H., and Barros, D.: Sources of concentric gravity waves
 821 generated by a moving mesoscale convective system in southern Brazil,
 822 Atmos. Chem. Phys., 22, 15153–15177, [https://doi.org/10.5194/acp-22-](https://doi.org/10.5194/acp-22-15153-2022)
 823 15153- 2022, 2022.

824 Parkinson, C. L.: Aqua: an Earth-Observing Satellite mission to examine water
 825 and other climate variables, IEEE Transactions on Geoscience and Remote
 826 Sensing, 41(2), 173-183, <https://doi.org/10.1109/TGRS.2002.808319>, 2003.

827 Piani, C., Durran, D., Alexander, M. J., and Holton, J. R.: A Numerical Study of
 828 Three-Dimensional Gravity Waves Triggered by Deep Tropical Convection
 829 and Their Role in the Dynamics of the QBO, J. Atmos. Sci., 57, 3689-3702,
 830 [https://doi.org/10.1175/1520-0469\(2000\)057%3C3689:ansotd%3E2.0.co;2](https://doi.org/10.1175/1520-0469(2000)057%3C3689:ansotd%3E2.0.co;2),
 831 2000.Picone, J. M., Hedin, A. E., Drob, D. P., and Aikin, A. C.: NRLMSISE-
 832 00 empirical model of the atmosphere: Statistical comparisons and scientific
 833 issues, J. Geophys. Res., 107, 1468, <https://doi.org/10.1029/2002JA009430>,
 834 2002.

835 Plane, J. M. C., Gumbel, J., Kalogerakis, K. S., Marsh, D. R., and von Savigny,
 836 C.: Opinion: Recent developments and future directions in studying the
 837 mesosphere and lower thermosphere, Atmos. Chem. Phys., 23, 13255–
 838 13282, <https://doi.org/10.5194/acp-23-13255-2023>, 2023.

839 Plougonven, R., and Zhang, F.: Internal gravity waves from atmospheric jets and

840 fronts, *Rev. Geophys.*, 52, 33-76, <https://doi.org/10.1002/2012RG000419>,
841 2014.

842 Pramitha, M., Venkat Ratnam, M., Taori, A., Krishna Murthy, B. V., Pallamraju,
843 D., and Vijaya Bhaskar Rao, S.: Evidence for tropospheric wind shear
844 excitation of high-phase-speed gravity waves reaching the mesosphere
845 using the ray-tracing technique, *Atmos. Chem. Phys.*, 15, 2709–2721,
846 <https://doi.org/10.5194/acp-15-2709-2015>, 2015.

847 Rothman, L. S., Gordon, I. E., Babikov, Y., Barbe, A., Chris Benner, D., Bernath,
848 P. F., Birk, M., Bizzocchi, L., Boudon, V., Brown, L. R., Campargue, A.,
849 Chance, K., Cohen, E. A., Coudert, L.H., Devi, V. M., Drouin, B. J., Fayt,
850 A., Flaud, J.-M., Gamache, R.R., Harrison, J. J., Hartmann, J.-M., Hill, C.,
851 Hodges, J. T., Jacquemart, D., Jolly, A., Lamouroux, J., Le Roy, R. J., Li, G.,
852 Long, D. A., Lyulin, O. M., Mackie, C. J., Massie, S. T., Mikhailenko, S.,
853 Müller, H. S. P., Naumenko, O.V., Nikitin, A. V., Orphal, J., Perevalov, V.,
854 Perrin, A., Polovtseva, E. R., Richard, C., Smith, M. A. H., Starikova, E.,
855 Sung, K., Tashkun, S., Tennyson, J., Toon, G. C., Tyuterev, V. G., and
856 Wagner, G.: The HITRAN2012 molecular spectroscopic database, *J. Quant.*
857 *Spectrosc. Radiat. Transfer*, 130, 4–50, [http://dx.doi.org/10.1016/](http://dx.doi.org/10.1016/j.jqsrt.2013.07.002)
858 [j.jqsrt.2013.07.002](http://dx.doi.org/10.1016/j.jqsrt.2013.07.002), 2013.

859 Russell, J. M. III, Mlynczak, M. G., Gordley, L. L., Tansock, J., and Esplin, R.:
860 An overview of the SABER experiment and preliminary calibration results.
861 *Proceedings of SPIE*, 3756, 277–288, <https://doi.org/10.1117/12.366382>,

1999.

Schmit, T. J., Gunshor, M. M., Menzel, W. P., Gurka, J. J., Li, J., and Bachmeier, A. S.: Introducing the next-generation advanced baseline imager on GOES-R, *Bull. Am. Met. Soc.*, 86, 1079-1096, <https://doi.org/10.1175/BAMS-86-8-1079>, 2005.

Schmit, T. J., Griffith, P., Gunshor, M. M., Daniels, J. M., Goodman, S. J., and Lebai, W. J.: A Closer Look at the ABI on the GOES-R Series. *Bulletin of the American Meteorological Society*, 98(4), 681–698, <https://doi.org/10.1175/bams-d-15-00230.1>, 2017 (data available at <https://www.ncdc.noaa.gov/airs-web/search>, last access: 10 December 2024).

Smith, S. M., Setvák, M., Beletsky, Y., Baumgardner, J., and Mendillo, M.: Mesospheric gravity wave momentum flux associated with a large thunderstorm complex, *Journal of Geophysical Research: Atmospheres*, 125, e2020JD033381, <https://doi.org/10.1029/2020JD033381>, 2020.

Smith, S. M., Vadas, S. L., Baggaley, W. J., Hernandez, G., and Baumgardner, J.: Gravity wave coupling between the mesosphere and thermosphere over New Zealand, *Journal of Geophysical Research-Space Physics*, 118(5), 2694–2707, <https://doi.org/10.1002/jgra.50263>, 2013.

Suzuki, S., Shiokawa, K., Otsuka, Y., Ogawa, T., Nakamura, K., and Nakamura, T.: A concentric gravity wave structure in the mesospheric airglow images, *Journal of Geophysical Research*, 112(D2), D02102.

884 <https://doi.org/10.1029/2005JD006558>, 2007a.

885 Suzuki, S., Shiokawa, K., Otsuka, Y., Ogawa, T., Kubota, M., Tsutsumi, M.,
886 Nakamura, T., and Fritts, D. C.: Gravity wave momentum flux in the upper
887 mesosphere derived from OH airglow imaging measurements, *Earth Planets*
888 *Space*, 59, 421–428, <https://doi.org/10.1186/BF03352703>, 2007b.

889 Swenson, G., and Mende, S. B.: OH emission and gravity waves (including a
890 breaking wave) in all-sky imagery from Bear Lake, UT, *Geophys. Res. Lett.*,
891 21, 2239–2242, <https://doi.org/10.1029/94GL02112>, 1994.

892 Swenson, G. R., and Liu, A. Z.: A model for calculating acoustic gravity wave
893 energy and momentum flux in the mesosphere from OH airglow,
894 *Geophysical Research Letters*, 25, 477–480,
895 <https://doi.org/10.1029/98GL00132>, 1998.

896 Swenson, G. R., Haque, R., Yang, W., and Gardner, C. S.: Momentum and energy
897 fluxes of monochromatic gravity waves observed by an OH imager at
898 Starfire Optical Range, New Mexico, *J. Geophys. Res.*, 104(D6), 6067–
899 6080, <https://doi.org/10.1029/1998JD200080>, 1999. Tang, Y., Dou, X., Li,
900 T., Nakamura, T., Xue, X., Huang, C., Manson, A., Meek, C., Thorsen, D.,
901 and Avery, S.: Gravity wave characteristics in the mesopause region
902 revealed from OH airglow imager observations over Northern Colorado, *J.*
903 *Geophys. Res. Space Physics*, 119, 630–645,
904 <https://doi.org/10.1002/2013JA018955>, 2014.

905 Vadas, S., Yue, J., and Nakamura, T.: Mesospheric concentric gravity waves

906 generated by multiple convective storms over the North American Great
 907 Plain, J. Geophys. Res., 117, D07113,
 908 <https://doi.org/10.1029/2011JD017025>, 2012.

909 Vargas, F., Chau, J. L., Charuvil Asokan, H., and Gerding, M.: Mesospheric
 910 gravity wave activity estimated via airglow imagery, multistatic meteor
 911 radar, and SABER data taken during the SIMONe-2018 campaign, Atmos.
 912 Chem. Phys., 21, 13631–13654, [https://doi.org/10.5194/acp-21-13631-](https://doi.org/10.5194/acp-21-13631-2021)
 913 2021, 2021.

914 Wrasse, C. M., Nyassor, P. K., da Silva, L. A., Figueiredo, C. A. O. B., Bageston,
 915 J. V., Naccarato, K. P., Barros, D., Takahashi, H., and Gobbi, D.: Studies on
 916 the propagation dynamics and source mechanism of quasi-monochromatic
 917 gravity waves observed over São Martinho da Serra (29° S, 53° W), Brazil,
 918 Atmos. Chem. Phys., 24, 5405–5431, [https://doi.org/10.5194/acp-24-5405-](https://doi.org/10.5194/acp-24-5405-2024)
 919 2024, 2024.

920 Wright, C. J., Hindley, N. P., Hoffmann, L., Alexander, M. J., and Mitchell, N. J.:
 921 Exploring gravity wave characteristics in 3-D using a novel S-transform
 922 technique: AIRS/Aqua measurements over the Southern Andes and Drake
 923 Passage, Atmos. Chem. Phys., 17, 8553–8575, [https://doi.org/10.5194/acp-](https://doi.org/10.5194/acp-17-8553-2017)
 924 17-8553-2017, 2017.

925 Wüst, S., Bittner, M., Espy, P. J., French, W. J. R., and Mulligan, F. J.: Hydroxyl
 926 airglow observations for investigating atmospheric dynamics: results and
 927 challenges, Atmos. Chem. Phys., 23, 1599–1618,

928 <https://doi.org/10.5194/acp-23-1599-2023>, 2023.

929 Wüst, S., Schmidt, C., Hannawald, P., Bittner, M., Mlynczak, M. G., and Russell
930 III, J. M.: Observations of OH airglow from ground, aircraft, and satellite:
931 investigation of wave-like structures before a minor stratospheric warming,
932 Atmos. Chem. Phys., 19, 6401– 6418, [https://doi.org/10.5194/acp-19-6401-](https://doi.org/10.5194/acp-19-6401-2019)
933 2019, 2019.

934 Xu, J., Li, Q., Yue, J., Hoffmann, L., Straka, W. C., Wang, C., Liu, M., Yuan, W.,
935 Han, S., Miller, S. D., Sun, L., Liu, X., Liu, W., Yang, J., and Ning, B.:
936 Concentric gravity waves over northern China observed by an airglow
937 imager network and satellites, J. Geophys. Res.-Atmos., 120, 11058–11078,
938 <https://doi.org/10.1002/2015JD023786>, 2015.

939 Yue, J., Vadas, S. L., She, C. Y., Nakamura, T., Reising, S. C., Liu, H. L., and Li,
940 T.: Concentric gravity waves in the mesosphere generated by deep
941 convective plumes in the lower atmosphere near Fort Collins, Colorado,
942 Journal of Geophysical Research, 114, D06104, [https://](https://doi.org/10.1029/2008JD011244)
943 doi.org/10.1029/2008JD011244, 2009.

944 Yue, J., Hoffmann, L., and Alexander, M. J.: Simultaneous observations of
945 convective gravity waves from a ground-based airglow imager and the
946 AIRS satellite experiment, J. Geophys. Res. Atmos., 118, 3178–
947 3191, <https://doi.org/10.1002/jgrd.50341>, 2013.